

Article

# Sedimentology, Provenance and Radiometric Dating of the Silante Formation: Implications for the Cenozoic Evolution of the Western Andes of Ecuador

Cristian Vallejo <sup>1,2,\*</sup>, Santiago Almagor <sup>1</sup>, Christian Romero <sup>3</sup>, Jose L. Herrera <sup>4,5</sup>,  
Vanessa Escobar <sup>1</sup>, Richard A. Spikings <sup>6</sup>, Wilfried Winkler <sup>7</sup> and Pieter Vermeesch <sup>4</sup>

<sup>1</sup> Departamento de Geología, Facultad de Ingeniería en Geología y Petróleos, Escuela Politécnica Nacional, Quito 170517, Ecuador; santiago.almagor@geostrats.com (S.A.); vanessa.escobar@epn.edu.ec (V.E.)

<sup>2</sup> Geostrat SA. Jorge Drom N39-188 y Jose Arizaga, Quito 170507, Ecuador

<sup>3</sup> Instituto de Investigación Geológico Energético (IIGE), Quito 170518, Ecuador; wladimir.romero@geoenergia.gob.ec

<sup>4</sup> Department of Earth Sciences, University College London, Gower Street, London WC1E 6BT, UK; josel.herrera@epoch.edu.ec (J.L.H.); p.vermeesch@ucl.ac.uk (P.V.)

<sup>5</sup> GIDAC, Instituto de Investigaciones, Escuela Superior Politécnica de Chimborazo, Riobamba 060155, Ecuador

<sup>6</sup> Department of Earth Sciences, University of Geneva, CH-1205 Geneva, Switzerland; Richard.Spikings@unige.ch

<sup>7</sup> Department of Earth Sciences, ETH-Zürich, CH-8092 Zürich, Switzerland; wilfried.winkler@erdw.ethz.ch

\* Correspondence: cristian.vallejov@epn.edu.ec; Tel.: +593-998726188

Received: 31 August 2020; Accepted: 10 October 2020; Published: 21 October 2020



**Abstract:** The Silante Formation is a thick series of continental deposits, exposed along a trench-parallel distance of approximately 300 km within the Western Cordillera of Ecuador. The origin, tectonic setting, age and stratigraphic relationships are poorly known, although these are key to understand the Cenozoic evolution of the Ecuadorian Andes. We present new sedimentological, stratigraphic, petrographic, radiometric and provenance data from the Silante Formation and underlying rocks. The detailed stratigraphic analysis shows that the Silante Formation unconformably overlies Paleocene submarine fan deposits of the Pilalo Formation, which was coeval with submarine tholeiitic volcanism. The lithofacies of the Silante Formation suggest that the sediments were deposited in a debris flow dominated alluvial fan. Provenance analysis including heavy mineral assemblages and detrital zircon U-Pb ages indicate that sediments of the Silante Formation were derived from the erosion of a continental, calc-alkaline volcanic arc, pointing to the Oligocene to Miocene San Juan de Lachas volcanic arc. Thermochronological data and regional correlations suggest that deposition of the Silante Formation was coeval with regional rock and surface uplift of the Andean margin that deposited alluvial fans in intermontane and back-arc domains.

**Keywords:** provenance analysis; Western Andes; Miocene; Silante Formation; Ecuador

## 1. Introduction

The Western Andes of Ecuador located between 1° N to 3° S along the active margin of South America (Figure 1) are composed of allochthonous oceanic blocks, which accreted in the late Cretaceous period [1,2]. The events of accretion are partly considered to influence orogenic processes, and the chemical composition of arc volcanism in the Northern Andes [3,4]. Previous studies of the Western Cordillera of Ecuador improved our understanding of the tectonic and stratigraphic evolution of this accretionary complex [5–11]. However, the Cenozoic sedimentary and tectonic evolution of the Western Andes of Ecuador remains poorly understood.

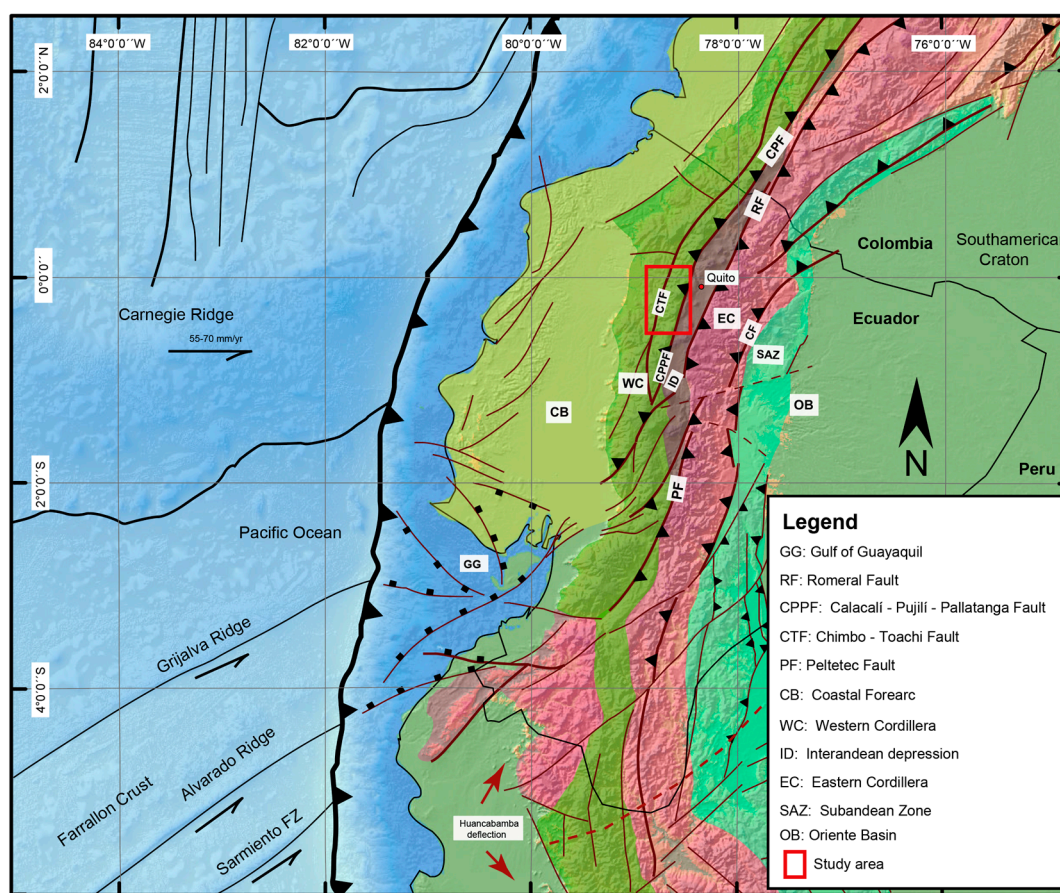


**Figure 1.** Lithotectonic map of Ecuador (modified from Luzieux et al. [1]) and location of the study area.

The Paleocene to Miocene period is particularly significant because several ore deposits formed over a large latitudinal range ( $0^{\circ}$  to  $3^{\circ}30'$  S) within the Western Cordillera during the Cenozoic (42–6 Ma; [12,13]). Thus, a reconstruction of the areal distribution and temporal framework of magmatism and its volcanic products will improve our understanding of the spatial distribution of mineral deposits.

The Silante Formation is a ~2000-m-thick series of red beds with intercalated conglomerates and sandstones rich in volcanic material [14]. It occupies a large area within the Western Cordillera, extending from  $1^{\circ}$  North to  $1^{\circ}$  South (Figure 2). The Silante Formation is intruded by mafic (diorite and andesite) dikes and sills [7,15]. Several authors have proposed different stratigraphic and geodynamic interpretations for the origin of these thick continental deposits [5–7,11–18]; however, the stratigraphic relationships of the Silante Formation remain unsolved, mainly because of the discontinuous rock exposures, and the absence of a coherent chronostratigraphic framework.

This study presents new sedimentological, stratigraphic, structural and geochronological data from several exposures of the Silante Formation and the underlying rocks. These data are used to determine the history of sedimentation and the tectonic regime. Radiometric dating and provenance studies including heavy minerals and single grain geochemistry are used to constrain the age, mineralogical composition and approximate location of the sediment source regions, which facilitates tectonic reconstructions and stratigraphic correlations [2]. This study addresses the geological evolution of a segment of the Western Cordillera of Ecuador and includes a detailed description of rock outcrops exposed along east to west road sections that traverse the Western Cordillera (Figure 2). These traverses are the Nono–Tandayapa, Calacalí–Nanegalito, Quito–Santo Domingo, Quito–Chiriboga and Otavalo–Selva Alegre road sections.

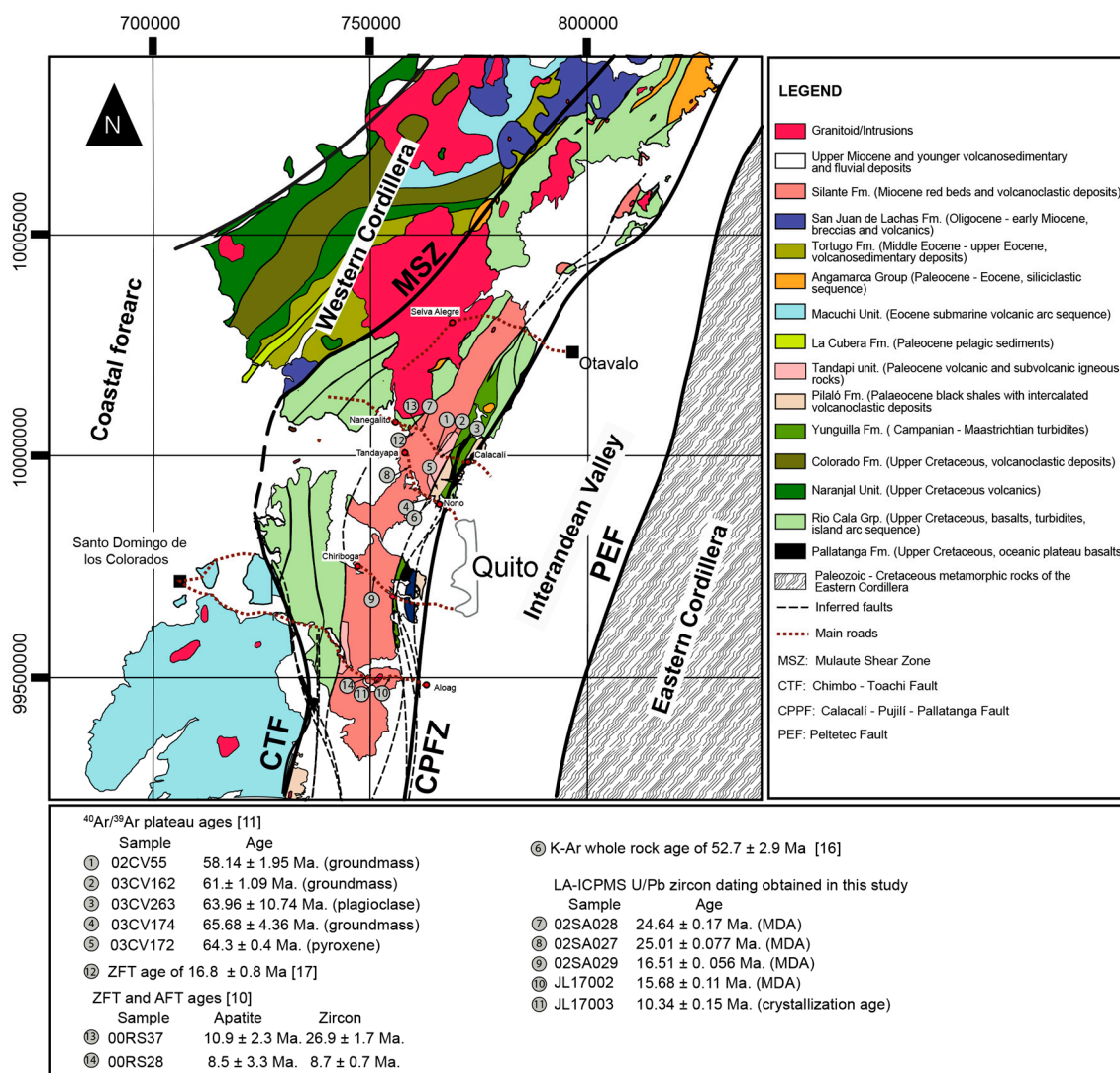


**Figure 2.** Geological map of the Western Cordillera from 1° North to 1° South, showing the main geological units (modified after [18]) and radiometric ages from the literature [10,11,16,17] and this study.

## 2. Regional Geology

Ecuador can be subdivided into five morphotectonic regions (Figure 1). (1) The coastal forearc is composed of mafic oceanic crust [1,3,19] and is covered by Paleogene to Neogene forearc deposits [2]. (2) The Western Cordillera (Figure 2) consists of mafic and intermediate extrusive and intrusive rocks that are tectonically juxtaposed with sedimentary rocks of Late Cretaceous to Miocene age [2,9,11]. (3) The Interandean Valley or Interandean Depression is located between the Western and Eastern cordilleras and is covered by thick Quaternary volcanic deposits [20], which are underlain by a crystalline basement composed of metamorphic and mafic rocks [20–22]. On its western flank, the Interandean Valley is bound by the Calacalí–Pujilí Fault [2,23]. This fault system (Figure 2) defines a suture between the South American continental margin and the accreted oceanic rocks [2,23]. (4) The Eastern Cordillera is formed by Paleozoic to Jurassic metamorphic rocks, and Mesozoic granitoids [10,24]. The Eastern Cordillera is separated from the Interandean Valley by the Pelletec Fault, which is the southward continuation of the Silvia-Pijao Fault of Colombia [22,25]. The east verging Cosanga Fault corresponds to the eastern limit of the Eastern Cordillera [24]. (5) The Oriente Basin is a Late Cretaceous–Quaternary retroarc foreland basin that developed on the South American plate margin in response to the weight of the adjacent Eastern Cordillera [26–28].

### 2.1. The Western Cordillera

The Western Cordillera of Ecuador consists of oceanic mafic rocks interpreted to have accreted to South America during the Late Cretaceous [2,19,29]. Sedimentary and volcano-sedimentary units overlying the allochthonous basement have a complex structural organization (Figure 2) due to the activity of NS striking faults [2,23]. The juxtaposition of turbidite successions and volcano-sedimentary rocks of similar lithologies albeit contrasting depositional ages has complicated stratigraphic correlations and tectonic reconstructions [2].

### 2.2. The Pallatanga Block and the Allochthonous Basement of Western Ecuador

The Pallatanga block corresponds to the allochthonous basement of the Western Cordillera of Ecuador and includes sedimentary and volcanic formations, which can be grouped into: (1) Basement rocks including basalts of the Pallatanga Formation and ultramafic rock of the San Juan complex (2) Late Cretaceous submarine basaltic lavas and volcanoclastic rocks of the Rio Cala arc; (3) Volcanic and subvolcanic rocks of the Tandapi unit of latest Maastrichtian to Paleocene age [2]; (4) Paleocene–Eocene submarine deposits of the Angamarca Group [23]; and (5) Oligocene–Miocene subaerial volcanic and volcanoclastic rocks of calc-alkaline affinity [2,18]. Oligocene–Miocene volcanism includes the San Juan de Lachas Formation in northern Ecuador [18,30], and the Saraguro Formation in southern Ecuador [31].

The Pallatanga Formation is the basement of the Western Cordillera and includes submarine basaltic lavas and dolerites. The basalts display flat primitive mantle- and chondrite-normalized REE patterns, very similar in chemical composition to basalts from the Caribbean Plateau [1,8], interpreted to have formed in an intraoceanic setting. Oceanic plateaus have thicknesses that are usually more than 10 km, and can exceed 30 km [32], which renders them difficult to subduct due to excessive positive buoyancy. Consequently, oceanic plateau fragments can be incorporated to the continental margin.

The San Juan ultramafic complex is exposed southwest of Quito and includes peridotites, dunites, and layered gabbros. REE geochemistry and isotopic data suggest that the San Juan complex represents the intrusive components of an oceanic plateau [2,33]. Radiometric ages obtained from gabbros of the San Juan complex include a zircon U-Pb age of  $87.1 \pm 1.7$  Ma [11], which is considered to be the most accurate estimate of the crystallization age of the oceanic plateau basement of the Western Cordillera.

### 2.3. The Yunguilla Formation

The Yunguilla Formation [34], is exposed on the eastern flank of the Cordillera Occidental (Figure 2) and lithologically includes relatively thin beds ranging from 10 to 20 cm in thickness, which display a rhythmic stratification pattern of massive siltstones and fine-grained sandstones that alternate with mudstones. The sandstones contain quartz and display  $T_{bde}$  turbidite subdivisions, interpreted as intermediate to distal parts of a submarine fan [17]. Mapping of the Yunguilla Formation along the Western Cordillera is sparse and is mostly based on lithological characteristics, therefore it can be confused with Paleocene and Eocene turbidites of the Angamarca Group.

The presence of ammonites *Phylloceras* sp. and *Exiteloceras* sp. suggest a Late Campanian to Early Maastrichtian age [9]. Heavy mineral assemblages in the Yunguilla Formation include zircon, tourmaline, rutile, garnet and epidote with minor amounts of titanite, anatase and brookite, which indicate significant input of granitic and metamorphic detritus, derived from the reworking of older formations of the present-day Eastern Cordillera [2]. The Yunguilla Formation was deposited in a north–south oriented forearc basin along the South American continental margin [2] and has a tectonic contact with the underlying Pallatanga Formation [23].

#### 2.4. The Tandapi Unit

The Tandapi unit [5] includes a sequence of volcanic rocks, tuffs and conglomerates exposed along the Alóag–Santo Domingo highway. Egüez [7] defined the Tandapi unit as a sequence of andesites and volcanic breccias in transitional contact with the overlying red beds of the Silante Formation.

Lithologically, the Tandapi unit corresponds to andesites and breccias, which have a greenish-grey stain, porphyritic texture and a fresh appearance [5]. The lavas are porphyritic andesites with plagioclase, hornblende and pyroxene within a pilotaxitic or hyalopilitic matrix, formed by microliths of plagioclase and alteration minerals. Isotopic data obtained from andesites and basalts of the Tandapi unit in the Alóag–Santo Domingo road indicate that the volcanic rocks erupted through isotopically juvenile rocks [22,35].

Egüez [7] proposed a Paleocene to Eocene age for the Tandapi unit because it was considered to overlie the Upper Cretaceous Pilaton Formation. Vallejo et al. [11] correlated the Tandapi unit with igneous rocks in contact with red beds of the Silante Formation along the Nono–Tandayapa and Calacalí–Nanegalito sections (Figure 4). These authors reported  $^{40}\text{Ar}/^{39}\text{Ar}$  plateau ages of  $58.1 \pm 1.95$  Ma (groundmass),  $61 \pm 1.09$  Ma (groundmass) and  $63.96 \pm 10.7$  Ma (plagioclase), suggesting that the volcanic rocks of the Tandapi unit were deposited during the late Maastrichtian to early Paleocene.

#### 2.5. The Angamarca Group and the Pilalo Formation

The Angamarca Group is a basin fill sequence composed of siliciclastic sedimentary rocks that include turbiditic sandstones, conglomerates and limestone intervals that were deposited from the Paleocene to Oligocene [17]. From base to top the Angamarca Group is subdivided into the Pilalo, Saquisilí, Apagua, Unacota and Rumi Cruz formations [17,22].

The Pilalo Formation was defined by Egüez and Bourgeois [36] as “Volcánicos Pilalo”. It contains coarse-grained turbiditic sandstones, black shales, siltstones, reworked tuffs and matrix supported breccias with andesitic fragments. Egüez and Bourgeois [36] reported a lower member of the Pilalo Formation that includes volcanic rocks with green and red detritus, and intercalated lavas, whereas the upper part includes calcareous siltstones. The Pilalo Formation is overlain by Eocene limestones of the Unacota Fm., which is interpreted as a concordant contact [7,22]. Vallejo [22] reported the presence of the Pilalo Formation to the northwest of Quito along the Nono–Tandayapa road section. At this locality, Savoyat et al. [37] described the foraminiferal fauna *Epigonal Rzehakina* within two samples collected near the Alambí River, which indicates a Paleocene age [22]. Vallejo [22] reported a  $^{40}\text{Ar}/^{39}\text{Ar}$  plateau ages of  $34.81 \pm 1.35$  Ma from an andesitic dyke that crosscuts marine sedimentary rocks of the Pilalo Formation, and  $65.68 \pm 4.36$  Ma (groundmass) from lavas at the top of the Pilalo Formation along the Nono–Tandayapa road section (Figure 2).

The Saquisilí Formation includes dark grey micaceous sandstones, siltstones and some calcareous strata [9,17] that were deposited as turbidites. The Saquisilí Formation is limited by faults to the East and West [17] and rests discordantly on pelagic chert of the Campanian-Maastrichtian Yunguilla Formation. Hughes and Bermudez [17] proposed an early to middle Paleocene age based on the presence of foraminifera microfossils collected close to the type locality.

The Apagua Formation overlies the Saquisilí Formation consists of medium-grained sandstones, siltstones and shales forming turbiditic beds. The sandstones contain quartz, mafic minerals, lithic fragments and feldspar [2,22]. Foraminiferal fauna from this unit indicate a middle Paleocene to middle Eocene age [17].

The Rumi Cruz unit is the youngest part of the Angamarca Group and includes quartz-rich sandstones with cross-stratification, red mudstones and massive conglomerates, that were probably deposited in a fan delta system [17]. The lithofacies association suggest that the Angamarca Group represents an upward-shallowing progradational succession that records a shift from a submarine fan to fan delta environment [2,22].

### 2.6. The Oligocene to Miocene San Juan De Lachas Continental Arc

The San Juan de Lachas Formation integrates matrix supported breccias with intercalations of andesitic lavas and volcanoclastic deposits. It unconformably overlies the volcanoclastic rocks of the Late Cretaceous Pilatón Formation [18] and is exposed in the northern part of the Western Cordillera (Figure 2). The San Juan de Lachas Formation was extensively analysed by Van Thournout [38] who reported a K-Ar age (hornblende) of 32.6 Ma from an andesitic dike that crosscuts a sequence of lava and agglomerates of similar composition. Boland [18] reported two K-Ar ages (hornblende) of  $19.8 \pm 3$  Ma and  $36.3 \pm 2$  Ma of andesites rich in hornblende and plagioclase. Samples collected in the Guayllabamba River yield zircon fission track ages of  $23.5 \pm 1.5$  Ma and  $24.5 \pm 3.1$  Ma [18]. Vallejo [22] obtained an  $^{40}\text{Ar}/^{39}\text{Ar}$  plateau age (hornblende) of  $32.9 \pm 1.2$  Ma, from an andesite collected east of the towns of Jijón and Caamaño. Geochemical analysis of the andesitic lavas shows that they are calc-alkaline in composition, and hence probably erupted in a continental arc setting [18,22].

### 3. The Silante Formation and Its Stratigraphic Problem

The Silante Formation is a continental sedimentary sequence, which includes volcanic-rich sandstones, conglomerates and red mudstones [14]. The Silante Formation is exposed along the Western Cordillera of Ecuador, from the Alóag–Santo Domingo road northward to the Colombian border [2]. Most of the sedimentary rocks of the Silante Formation have experienced very little transport, as revealed by high angularity and poor sorting of crystal grains and the clasts [2,17]. The volcanic-rich sandstones have a purple color and contain crystalline fragments of plagioclase, pyroxene, hornblende, zircon, quartz and abundant lithic fragments. Clasts in conglomerates of the Silante Formation are lithologically similar to the Yunguilla, Rio Cala and Pallatanga formations, suggesting reworking of older sedimentary and volcanic rocks [2]. A three-meter sequence of yellow laminated shales, with the presence of well-preserved angiosperm leaves are reported by Boland et al. [18] in the Calacalí–Nanegalito section. The laminated shales were deposited in a terrestrial environment [18].

There are significant differences in the stratigraphic position, age and depositional environment attributed by different authors (Figure 3). Savoyat et al. [37] proposed a Paleocene age for the Silante Formation based on the presence of foraminifera *Gaudryina* aff. *laevigata* Franke, *Globotruncana* sp. and *Cibicides* sp., which were found in the Silante Formation and were presumably reworked from the Paleocene Pilalo Formation. Henderson [6] indicated the presence of lavas at the top of the Silante Formation and mentions that base and top criteria would indicate that the Silante Formation is covered by the Yunguilla Formation along the Nono–Tandayapa road section (Figure 3). However, the base and top criteria are not clearly described or shown with photographic or stratigraphic evidence. Kehrer and Van der Kaaden [5] proposed a Paleocene to early Eocene age for the Silante Formation and correlated it with Paleocene molasse type deposits of the Tiyuyacu Formation of eastern Ecuador.

Egüez [7] proposed that Silante Formation is transitionally overlying the Tandapi Unit along the Quito–Santo Domingo road, and was contemporary with submarine deposits of the Eocene Apagua Formation. This author also observed the presence of reworked detrital elements in the conglomerates of the Silante Formation, whose lithologies correspond to calc-alkaline lavas similar to the Tandapi unit. The transitional contact between the Tandapi unit and the Silante Formation proposed by Egüez [7] was questioned by Van Thournout [38], who reinterpreted the sequence of lavas and breccias of the Silante Formation and suggest they were deposited during the Oligocene.

The Silante Formation was redefined by Hughes and Bermudez [17] and Boland et al. [18]. These authors included within the Silante Formation andesites, dacites and volcanic breccia intercalations of calc-alkaline affinity, together with the continental red-bed sequence. The non-tectonic contact between the Silante Formation and the mapped Yunguilla Formation along the Calacalí–Nanegalito road was interpreted as a depositional hiatus (paraconformity), suggesting the Silante Formation is post-Maastrichtian (Figure 3).

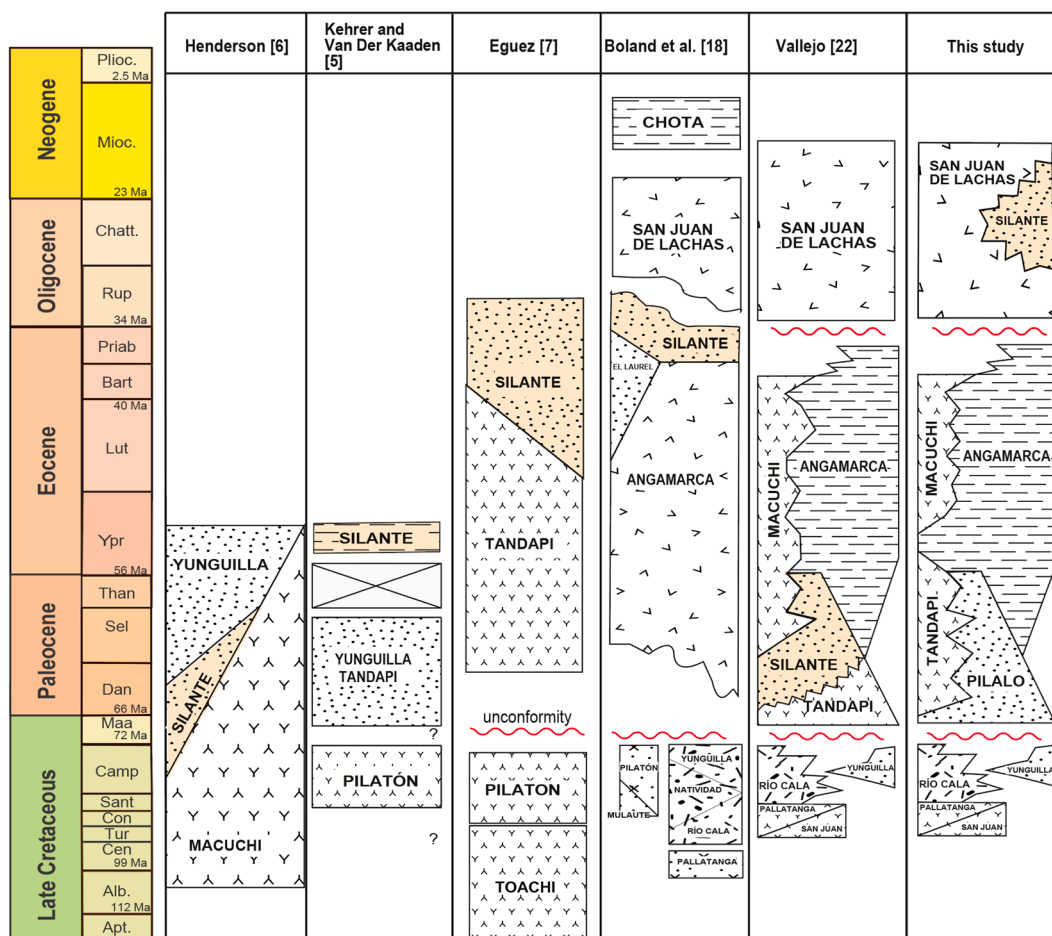


**Figure 3.** Stratigraphic position of the Silante Formation according to different authors [5–7,18,22]. Time scale from Cohen et al. [39].

Wallrabe-Adams [16] reported a K-Ar age of  $52.7 \pm 2.9$  Ma (whole rock) from a lava collected along the Nono–Tandayapa road. The rock is interpreted to represent the top of the Silante Formation by the author. Hughes and Bermudez [17] assigned a depositional age of  $16.8 \pm 0.8$  Ma, in which is a zircon fission track date obtained from sedimentary rocks collected along the Calacalí–Nanegalito road.

Vallejo [22] obtained  $^{40}\text{Ar}/^{39}\text{Ar}$  plateau ages (groundmass and plagioclase) from igneous rocks mapped by Boland et al. [18] within the Silante Formation. Based on the  $\sim 65.68$  to  $58.1$  Ma obtained from these rocks, this author proposed that the Silante Formation was deposited during the Maastrichtian to early Paleocene times (Figure 3).

#### 4. Methodology

Fifteen sandstone samples were used for the study of heavy minerals (Table 1). The sandstones were treated following standard laboratory procedures, which included crushing, sieving and density separation [40,41] using sodium polytungstate (density =  $2.89 \text{ g/cm}^3$ ). The heavy minerals were mounted on glass slides using piperine (refractive index = 1.68).

**Table 1.** Sample locations, and analysis performed in this study.

Sample	Latitude	Longitude	Area	Formation	Lithology	Analysis			
						Heavy Minerals	Clinopyroxene Geochemistry	QFL Analysis	U-Pb Dating
00RS26	0°25'6.94" S	78°47'27.77" W	Aloag–Santo Domingo road	Silante	volcaniclastic sandstone		X		
JL17003	0°26'25.22" S	78°44'8.25" W	Aloag–Santo Domingo road	Silante	quartzdiorite				X
JL17002	0°26'18.81" S	78°42'24.19" W	Aloag–Santo Domingo road	Silante	volcaniclastic sandstone				X
01SA005	0°26'19.14" S	78°42'23.48" W	Aloag–Santo Domingo road	Silante	volcaniclastic sandstone	X		X	
01SA008	0°26'19.14" S	78°42'23.48" W	Aloag–Santo Domingo road	Silante	volcaniclastic sandstone			X	
02CV135	0°26'50.16" S	78°42'45.58" W	Aloag–Santo Domingo road	Silante	volcaniclastic sandstone			X	
00RS34	0°0'22.84" N	78°34'48.29" W	Calacali–Nanegalito road	Pilalo	volcaniclastic sandstone	X	X		
00RS35	0°0'22.52" N	78°35'27.44" W	Calacali–Nanegalito road	Pilalo	volcaniclastic sandstone		X		
02CV56	0°1'14.72" N	78°36'44.37" W	Calacali–Nanegalito road	Silante	volcaniclastic sandstone		X		
04SA049	0°1'19.56" N	78°36'52.71" W	Calacali–Nanegalito road	Silante	volcaniclastic sandstone	X		X	
02SA028	0°1'28.45" N	78°39'1.23" W	Calacali–Nanegalito road	Silante	volcaniclastic sandstone				X
04SA042	0°0'24.21" N	78°35'28.54" W	Calacali–Nanegalito road	Pilalo	volcaniclastic sandstone	X			
04SA053	0°0'14.16" N	78°35'22.04" W	Calacali–Nanegalito road	Pilalo	volcaniclastic sandstone	X		X	
04SA034	0°2'0.05" N	78°40'51.36" W	Calacali–Nanegalito road	Silante	volcaniclastic sandstone			X	
04SA051	0°1'29.39" N	78°37'5.60" W	Calacali–Nanegalito road	Silante	volcaniclastic sandstone			X	
00RS4	2°39'31.22" S	79°26'47.30" W	Cuenca–La Troncal road	Yunguilla	arkose sandstone	X			
00RS2	2°38'59.85" S	79°26'55.05" W	Cuenca–La Troncal road	Yunguilla	arkose sandstone	X			
WW3311	3°5'7.77" S	79°0'29.94" W	Cumbe	Yunguilla	arkose sandstone	X			
03CV172	0°1'49.69" S	78°33'35.47" W	Nono	Pilalo	andesite		X		
02SA027	0°1'55.20" S	78°38'30.84" W	Nono–Tandayapa road	Silante	volcaniclastic sandstone	X			X
05SA075	0°1'25.03" S	78°38'43.42" W	Nono–Tandayapa road	Silante	volcaniclastic sandstone	X			

Table 1. Cont.

Sample	Latitude	Longitude	Area	Formation	Lithology	Analysis			
						Heavy Minerals	Clinopyroxene Geochemistry	QFL Analysis	U-Pb Dating
02SA016	0°3'30.12" S	78°36'41.58" W	Nono–Tandayapa road	Pilalo	volcaniclastic sandstone	X			
02SA019	0°3'22.02" S	78°36'56.84" W	Nono–Tandayapa road	Pilalo	volcaniclastic sandstone	X			
05SA066	0°3'21.69" S	78°36'55.48" W	Nono–Tandayapa road	Pilalo	volcaniclastic sandstone			X	
05SA072	0°1'54.91" S	78°38'30.55" W	Nono–Tandayapa road	Silante	volcaniclastic sandstone			X	
05SA074	0°1'25.03" S	78°38'43.42" W	Nono–Tandayapa road	Silante	volcaniclastic sandstone			X	
02CV99	0°16'37.91" N	78°27'40.76" W	Otavaló–Selva Alegre road	Silante	volcaniclastic sandstone		X	X	
CV380	0°17'6.93" N	78°29'58.32" W	Otavaló–Selva Alegre road	Silante	volcaniclastic sandstone			X	
02SA029	0°16'42.49" S	78°42'31.86" W	Quito–Chiriboga road	Silante	volcaniclastic sandstone	X			X
06SA081	0°16'43.63" S	78°42'59.28" W	Quito–Chiriboga road	Silante	volcaniclastic sandstone	X		X	
02CV33	0°17'51.60" S	78°38'56.46" W	Quito–Chiriboga road	Pilalo	volcaniclastic sandstone	X			
06SA078	0°16'42.49" S	78°42'31.86" W	Quito–Chiriboga road	Silante	volcaniclastic sandstone			X	

X symbol in the table corresponds to the analysis performed to each sample.

Heavy mineral identification was made based on the optical properties of individual minerals, using a transmitted light Zeiss Primotech microscope. The mineral proportions were estimated by counting 300 detrital grains, following the procedure described by Mange and Maurer [40].

The provenance analysis of this study included the petrographic modal analysis of 14 sandstones, determining the relative proportions of detrital grains, which can be used to estimate the tectonics and paleogeography of the source regions [42,43]. The detrital components have been divided into feldspar (F), total quartz (Q), polycrystalline quartz (Qp), monocrystalline quartz (Qm), total lithic (Lt = L + Qp), lithic fragments (L), metamorphic lithic fragments (Lm), sedimentary lithic fragments (Ls), and volcanic lithic fragments (Lv). A total of 300 points were counted for each thin section using the Gazzi-Dickinson point-counting method [44,45]. The detrital components were plotted in QmFLt, QFL and LvLmLs ternary discrimination diagrams proposed by Dickinson et al. [46] and Dickinson [43]. Analyses were performed at the Petrology Laboratory of the Escuela Politécnica Nacional, Quito, Ecuador.

Single grain clinopyroxenes geochemistry was used to define the volcanic affinity of the volcanoclastic rocks of the Pilalo and Silante formations. Clinopyroxene grains were separated from the heavy mineral concentrates using a Frantz magnetic separator. Individual grains were mounted in an epoxy capsule and analyzed for major oxides and REE at ETH-Zürich [22]. Rock samples were mechanically and chemically disaggregated and processed according to standard heavy mineral separation techniques [28,40,41]. U-Pb ages of detrital zircons were obtained from four sandstones of the Silante Formation and from an intrusion that crosscuts this formation. Zircons were picked up from the non-magnetic fraction of the heavy minerals. Each sample was analyzed in a multi-selector laser-coupled plasma-mass spectrometer (LA-ICP-MS) at the University College London (UCL). All ages were obtained using a New Wave 193 nm aperture-imaged frequency-quintupled laser ablation system coupled to an Agilent 7700 quadrupole-based ICP-MS (Agilent Technologies, Santa Clara, CA, USA). Operating condition for zircon dating uses an energy density of ca 2.5 J/cm<sup>2</sup> and a repetition rate of 10 Hz. Repeated measurements of external zircon standard Plešovice [47] and NIST 612 silicate glass [48] are used to correct for instrumental mass bias and depth-dependent inter-element fractionation of Pb, Th and U. 91500 zircon [49] was used as secondary age standard. Data were processed using GLITTER data reduction software (v. 4.4, Gemoc, Sydney, Australia). Final data processing, statistical processing and graphs development were done using the software IsoplotR (v. 3.3, UCL, London, UK) online mode [50].

Maximum depositional ages for the Silante Formation were calculated using the minimum age model of Galbraith [51], included with the radial plot functionality of RadialPlotter [52] and IsoplotR [50]. The radial plot is a graphical device that was also invented by Galbraith [53] with the aim to simultaneously visualize measurements and their uncertainties. The minimum age calculation algorithm of Galbraith [51] converges to a specific value with increasing sample size.

## 5. Results

### 5.1. Stratigraphy of the Nono–Tandayapa and Calacalí–Nanegalito Road Sections

The Nono–Tandayapa and Calacalí–Nanegalito road sections include almost continuous exposures of the Silante Formation and underlying series. In these sections Boland et al. [18] assumed a non-tectonic contact between the Yunguilla and Silante formations. This contact was interpreted as a possible depositional hiatus (discordance). However, biostratigraphic studies based on foraminiferal fauna collected in the Alambi River by Savoyat et al. [36] yielded a Paleocene age (Danian) for sedimentary rocks mapped as the Yunguilla Formation. Therefore, Vallejo [22] discarded the presence of the Yunguilla Formation and proposed that the Paleocene rocks exposed in this area are correlatable with the Paleocene Pilalo Formation rather than the Yunguilla Formation. In this study, we follow the stratigraphy proposed by Vallejo [22] and present new stratigraphic and sedimentological data from the Nono–Tandayapa and Calacalí–Nanegalito road sections (Figure 4).

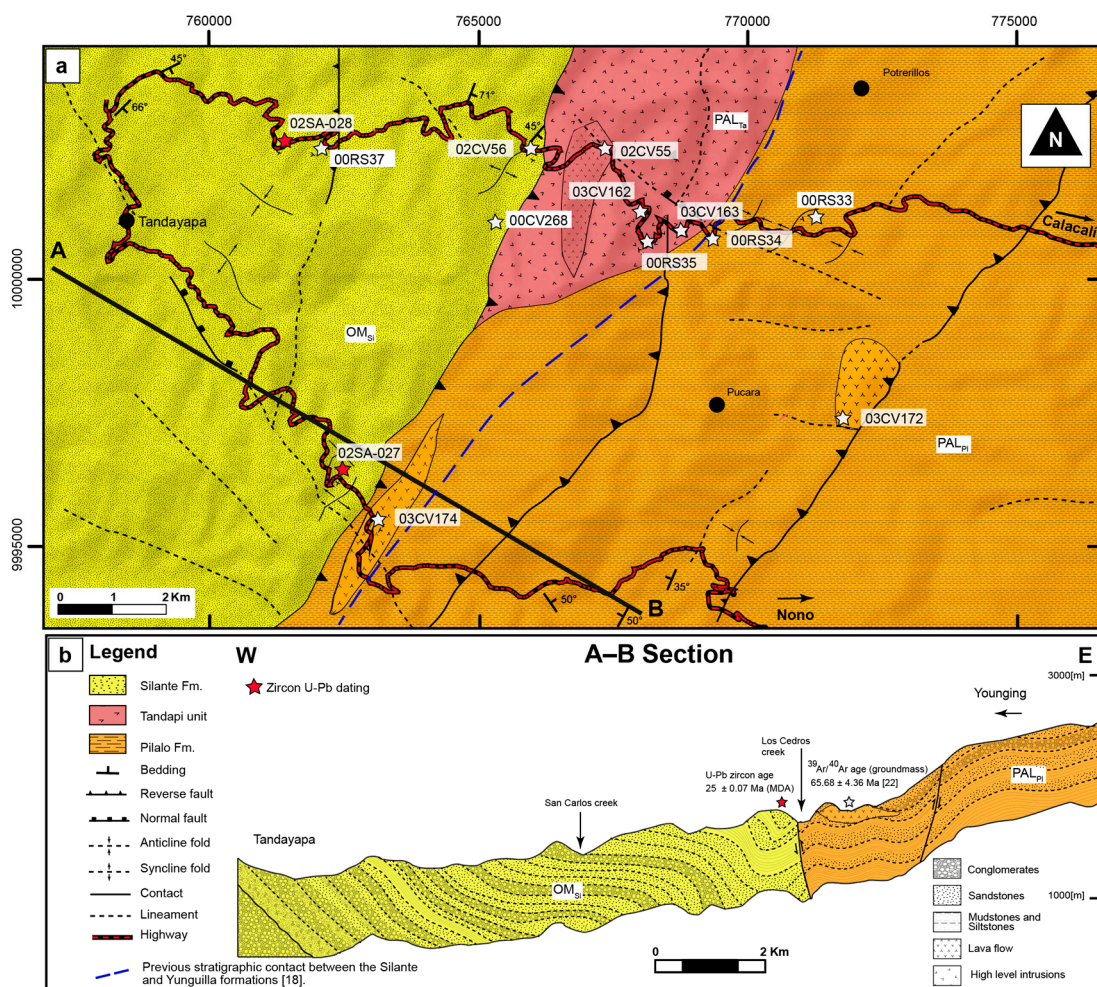


**Figure 4.** (a) Geological map of the area of study, and (b) schematic cross sections of the Nono–Tandayapa road section.

The western series along the Nono–Tandayapa road section corresponds to the Silante Formation (Figure 4), while the central series is an igneous sequence (Tandapi unit) that intrudes a submarine sedimentary sequence of ~1000 m in thickness, ascribed to the Pilalo Formation. In the analyzed road sections, there is a tectonic contact between the Silante Formation and the Tandapi unit, which is located between UTM 766182/2365 and 766106/2020 on the Calacalí–Nanegalito road (Figure 4). In the Nono–Tandayapa section the tectonic contact between the Pilalo Formation and the Silante Formation is located at los Cedros Creek (UTM 763032/9995645).

The Pilalo Formation is a coarsening-upwards submarine succession exposed at the eastern border of the studied section (Figure 5). The sedimentary rocks are folded and intercalated with lavas at the top. The intercalated andesitic to basaltic lavas yield a  $^{39}\text{Ar}/^{40}\text{Ar}$  plateau age (groundmass) of  $65.68 \pm 4.36$  Ma [2] that is coeval (within uncertainty) with the host sedimentary rocks.

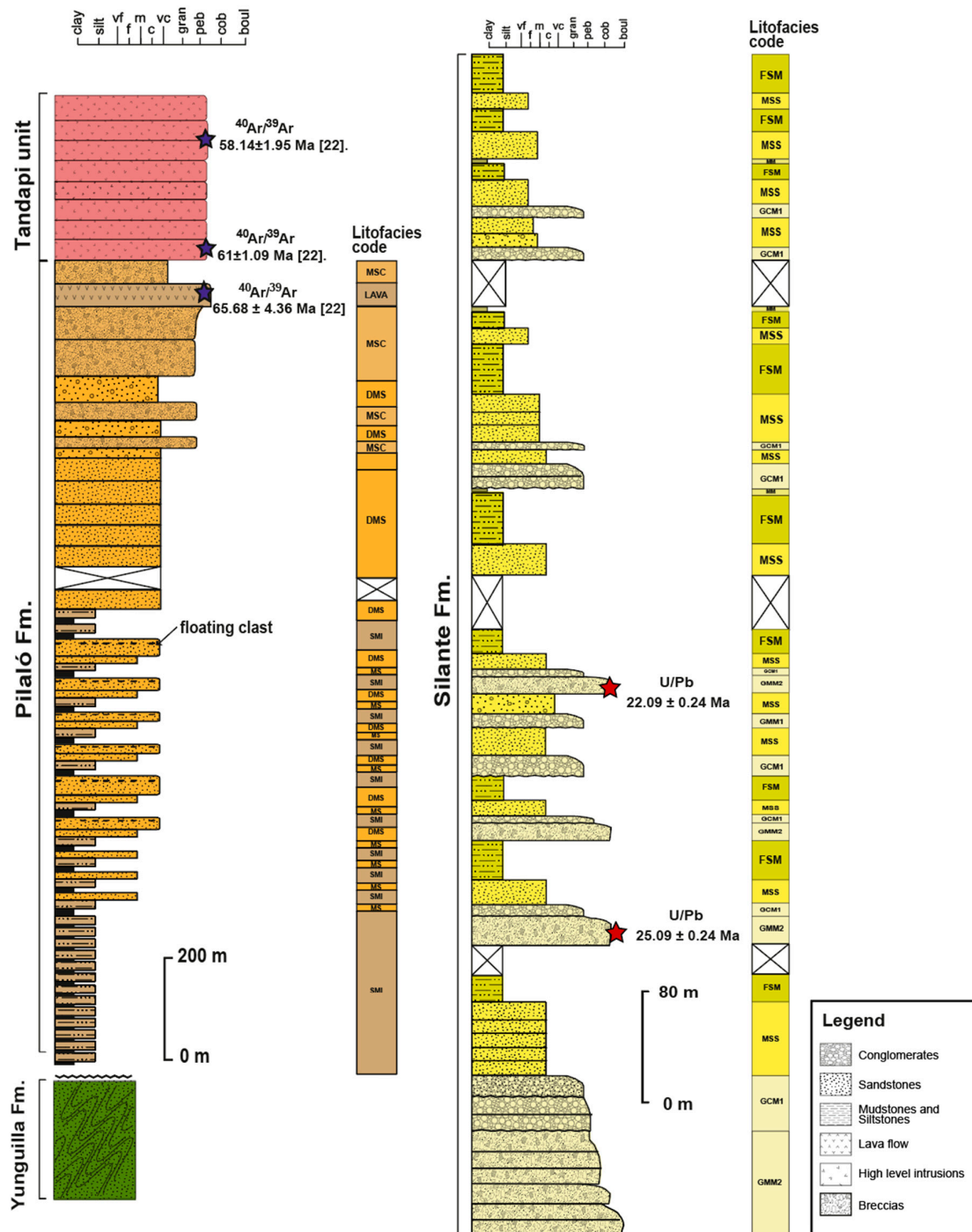


**Figure 5.** Composite stratigraphic column of the Nono–Tandayapa road section with lithofacies described for the Pilalo and Silante formations (lithofacies codes are discussed in text). Radiometric ages obtained by Vallejo [22] and this study are located with the proposed composite stratigraphic column of the study area.

The rocks at the top of the sedimentary sequence of the Pilalo Formation have a reddish color due to oxidation, and thus they were previously mapped as the Silante Formation [18]. However, they resemble turbidite beds falling out from highly concentrated flows with Bouma T<sub>ade</sub> subdivisions.

Porphyry type high level intrusions mapped as part of the Tandapi unit crosscut the Pilalo Formation close to the contact with the Silante Formation (Figure 4). Vallejo [22] reported <sup>39</sup>Ar/<sup>40</sup>Ar

plateau ages of two samples collected in the Calacalí–Nanegalito road (Figure 2) that yielded ages of  $61 \pm 1.09$  Ma (groundmass) and  $63.96 \pm 10.74$  Ma (plagioclase).

Our structural, biostratigraphic and radiometric ages obtained along the Calacalí–Nanegalito and Nono–Tandayapa sections suggest that the previous stratigraphic contact between the Silante and Yunguilla Formation, as proposed by Boland [18], does not exist. Sedimentary rocks of the Yunguilla Formation were not identified in the present study area. Instead, the Pilalo Formation together with the high-level intrusion of the coeval Tandapi unit were thrust onto the Silante Formation.

### 5.2. Sedimentology of the Pilalo Formation

The Pilalo Formation exposed along the Calacalí–Nanegalito and Nono–Tandayapa road sections is a thick sequence composed of sedimentary rocks deposited in a submarine environment. The bed-sets show an upward-coarsening and thickening trend, suggesting a progradational sequence stratigraphic pattern (Figure 5). In the Pilalo Formation, we identified four lithofacies, which are described in the following section. The acronym indicates the dominant lithology and the most important sedimentological features (Table 2).

**Table 2.** Lithofacies of the Pilalo and Silante formations.

Lithofacies	Description	Interpretation
<b>Pilalo Formation</b>		
SMI	Intercalations of dark grey laminated siltstones and mudstones	Silty-muddy turbidites (Bouma T <sub>de</sub> subdivisions) generated by low-density turbidity currents in the distal part of a submarine fan
MS	Massive sandstones with load cast, and volcanic clasts	Sandy turbidites generated by high-density turbidity current infilling channels in the middle part of a submarine fan
DMS	Massive sandstones with floating clasts of volcanic origin	Sandy debrites deposited by plastic flows in channels of the middle part of a submarine fan
MSC	Matrix-supported conglomerates with volcanic clasts	Conglomerates generated by debris flows. The common association with turbidites and sandy debrites suggests the upper part of a submarine fan
<b>Silante Formation</b>		
MM	Reddish unstructured mudstones and siltstones with poorly developed parallel lamination.	Reddish color in mudstones suggest floodplain deposits deposited under oxidizing conditions
FMS	Reddish siltstones and fine-grained sandstones	Distal facies of alluvial fan margins in semi-arid continental environments
MSS	Structureless fine-grained sandstones	Sandy lithofacies deposited by a hyper-concentrated flow in the middle part of an alluvial fan
SPL	Reddish to yellowish sandstones with parallel lamination	Channels or sheet flood deposits deposited in the middle part of an alluvial fan
GMM1	Massive matrix-supported conglomerates	Deposits produced by debris flows in the upper part of an alluvial fan
GCM1	Massive clast-supported conglomerates	Deposits formed by debris flows in the upper part of an alluvial fan system
GMM2	Matrix-supported conglomerates, poorly sorted	Proximal facies of an alluvial fan depositional system, close to the alluvial fan head

#### 5.2.1. Lithofacies SMI: Siltstones with Mudstone Intercalations

The lithofacies consists of a sequence of rhythmically bedded dark grey mudstone with siltstones (Figure 6a). The siltstones show parallel lamination and the beds range in thickness from 10 to 20 cm. Sporadic calcareous cement is also observed in this lithofacies. Some of these beds are rich in marine microfossil fauna, which are mostly foraminifera. This lithofacies dominates the lower part of the succession (Figure 5).

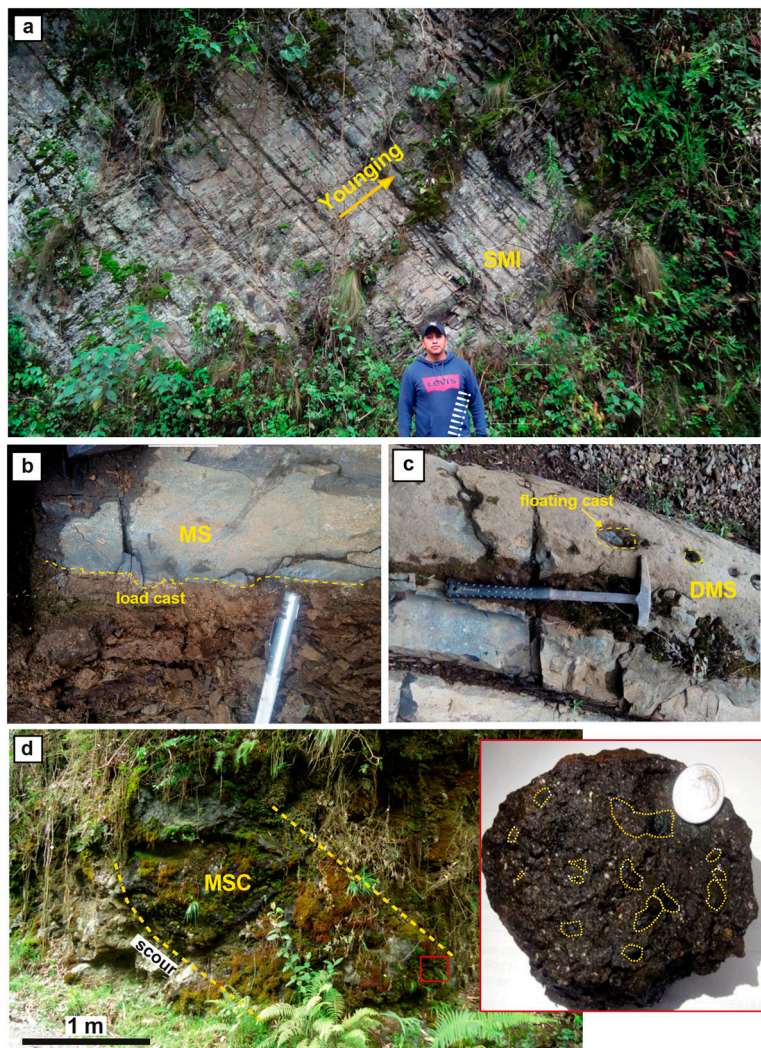


**Figure 6.** Photographs of representative lithofacies of the Pilalo Formation. (a) Lithofacies SMI, siltstone with mud intercalations; (b) lithofacies MS, structureless sandstones; (c) lithofacies DMS, massive sandstone with floating clasts; (d) lithofacies MSC, matrix supported conglomerates.

Parallel lamination could be a result of two main processes: (1) decelerating turbidity currents [54,55], or (2) bottom-current reworking [56,57]. The presence of parallel laminated siltstones with mudstone intercalations suggests silty-muddy turbidites (Bouma  $T_{de}$  subdivisions) that were generated by low-density turbidity currents in the distal part of a submarine fan [57].

### 5.2.2. Lithofacies MS: Massive Sandstones with Load Cast

Lithofacies MS consists of medium to coarse-grained sandstones composed of plagioclase, pyroxene and amphibole, which are accompanied by a few dark-colored siltstones, and green mudstone intrabasinal lithic fragments (Figure 6b). The bed thickness of this lithofacies varies between 0.5 to 1 m. The base of the sandstone beds displays load cast, and ball-and-pillow structures.

The presence of load cast and ball-and-pillow structures suggest rapid deposition of water-rich sediment by high-density turbidity currents (Bouma  $T_a$  subdivisions). Presumably, they represent fill deposits in channels in a middle fan environment [55,57]. The presence of plagioclase, pyroxene and amphibole suggests a volcanic source. The green color of the mudstones is a result of alteration of volcanic glass to chlorite.

### 5.2.3. Lithofacies DMS: Massive Sandstones with Floating Clasts

This lithofacies is characterized by medium to coarse-grained sandstone beds that are 0.3 to 0.8 m thick, with a massive structure. The sandstones are green and include plagioclase, pyroxene, chlorite and epidote crystals. It is common to find angular and sub-rounded volcanic and sedimentary floating clasts. The main characteristic of this lithofacies are intrabasinal floating clasts occurring at the top of the beds (Figure 6c).

Massive sands with floating clasts are either deposited by (1) high-density turbidity currents [58], or (2) sandy debris flows where the transport mechanism is a plastic flow and deposition is caused by mass freezing of sediments [59]. The abrupt freezing of the sediments impedes settling of the clasts towards the bottom of the stratum. Floating clasts in sandstones interspersed with siltstones and mudstones can be deposited by plastic flows defined as sandy debris flows [60]. This lithofacies represents infilling deposits of channels in a middle fan environment. The presence of plagioclase and pyroxene suggests a volcanic source. Epidote and chlorite formed via the alteration of mafic minerals and volcanic glass, respectively.

### 5.2.4. Lithofacies MSC: Matrix-Supported Conglomerates

Lithofacies MSC is characterized by the presence of green, matrix-supported conglomerates with subangular, partially oxidized andesitic clasts, with clast sizes that vary from pebbles to granules, and bed thickness that span between 1 to 2 m. The base of these deposits is erosive, forming a scour surface on top of the underlying beds (Figure 6d). The matrix of the conglomerates is composed of coarse-grained sandstone carrying plagioclase, amphibole, chlorite and epidote crystals.

The angularity of the clasts and the poorly sorted nature of the deposit reveals that they have not been transported over long distances. The structureless nature, together with the immaturity of clasts suggest a deposit generated by debris flows [61]. These flows are erosive and channelized, forming scoured lower contacts, and settled very rapidly, resulting in massive and ungraded beds [62]. The association with sandy debrites and turbidite beds (lithofacies DMS and MS) suggests that MSC lithofacies was formed within a submarine upper fan environment [60]. The mineralogy of the matrix and the clast lithology suggest a volcanic source.

## 5.3. Sedimentology of the Silante Formation

Alluvial fan sedimentary rocks of the Silante Formation are exposed along the Nono–Tandayapa and Calacalí–Nanegalito sections. We recognized 7 lithofacies in the Silante Formation, which has a thickness of approximately 900 m in this region (Figure 5).

### 5.3.1. Lithofacies MM: Mudstones

This lithofacies includes reddish couples of mudstones and siltstones (Figure 7a) with an approximate thickness that range from 1 to 3 cm. The mudstones are unstructured, and the siltstones include poorly developed parallel lamination. The beds have a tabular geometry and sharp basal contacts. This lithofacies occurs intercalated with the FMS lithofacies (see below).

The reddish color of the mudstones suggests subaerial deposition in a terrestrial environment under oxidizing conditions. Parallel lamination in the siltstones suggests they are floodplain deposits, which can develop in an inactive part of the alluvial fan system that occasionally receives sediment during flood events [63].

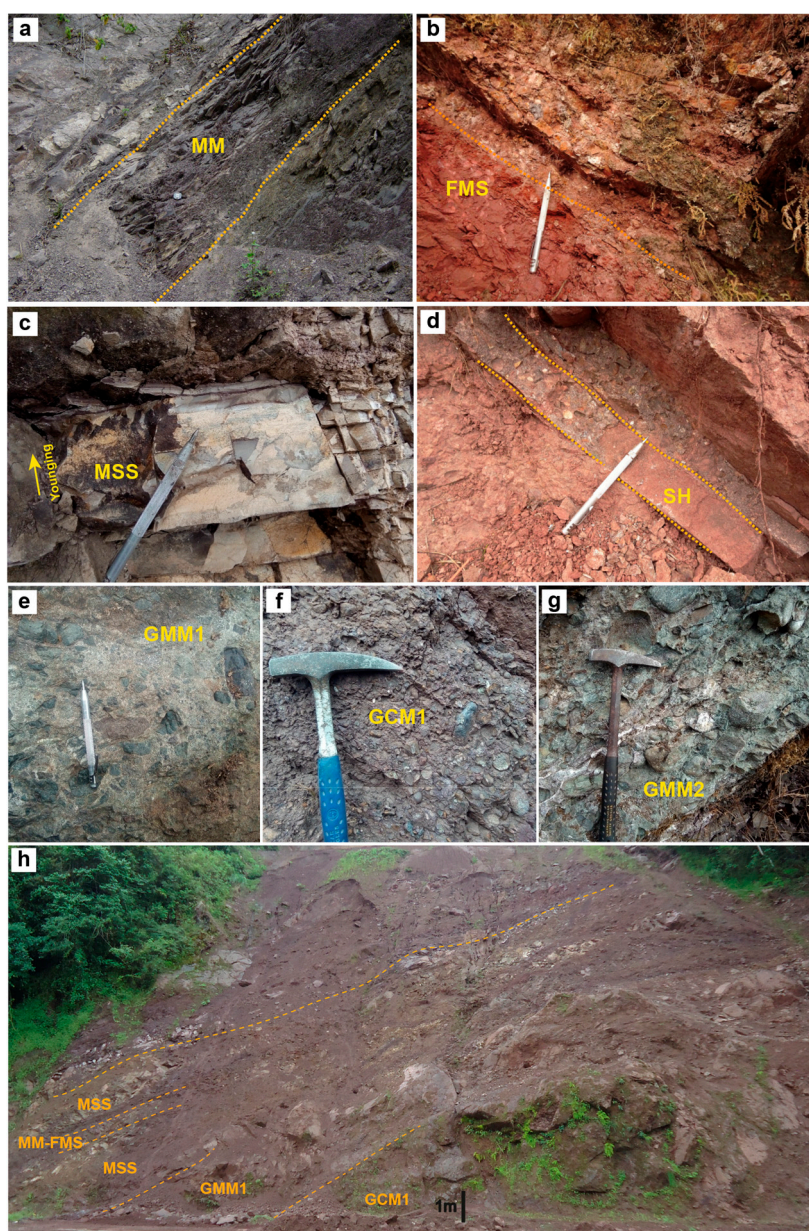


**Figure 7.** Photographs of representative lithofacies of the Silante Formation. (a) Lithofacies MM, mudstones and siltstone; (b) lithofacies FMS, structureless sandstones; (c) lithofacies MSS, massive sandstone; (d) lithofacies SH, matrix supported conglomerates; (e) lithofacies GMM1, massive matrix supported conglomerates; (f) lithofacies GCM1, massive clast supported conglomerates; (g) lithofacies GMM2, matrix supported conglomerates; (h) representative outcrop of the Silante Formation and the spatial distribution of the lithofacies.

### 5.3.2. Lithofacies FMS: Massive Siltstones

The FMS lithofacies consists of reddish, unstructured beds that vary in grain size from silt to fine-grained sandstones (Figure 7b), with bed thicknesses that range from 0.3 to 0.8 m. Individual beds are tabular and associated with lithofacies MM.

The reddish siltstones and very fine-grained sandstones may represent distal facies of an alluvial fan in a semi-arid continental environment [64–66]. The presence of thin beds of fine-grained lithofacies suggests that they are distal facies of abandoned progradational lobes [64]. The association of silt and

very fine sandstones (FMS) suggests deposition within quiet segments of alluvial fans, with sediments supplied during occasional flood events [67,68].

### 5.3.3. Lithofacies MSS: Massive Sandstones

The MSS lithofacies contains poorly sorted, ungraded fine sandstone beds with thicknesses up to 1 m and a tabular geometry (Figure 7c). The most abundant minerals within the sandstones are plagioclase, magnetite and mafic minerals, including pyroxene and amphibole. This lithofacies is usually associated with the FMS and MM lithofacies.

The unstructured sandstones were probably deposited from hyper-concentrated flows that were characterized by very high sediment to water ratios [69]. The lack of internal sedimentary structure in these poorly sorted sandstones suggest an abrupt deceleration and quick deposition of sediment with insufficient time to create bedforms [64,70]. This lithofacies commonly occurs within middle alluvial fans proximal to the mountain front, where the flow becomes unconfined, dewatered, and rapidly settles [71].

### 5.3.4. Lithofacies SPL: Sandstones with Parallel Lamination

The lithofacies SPL consists of reddish to yellow stained sandstones (Figure 7d), with grain sizes that vary from coarse to very coarse (0.5 to 2 mm). The sandstones have parallel lamination and are composed of plagioclase, pyroxenes, amphiboles and magnetite crystals.

The reddish color is considered to be a consequence of deposition in an oxidizing environment [72,73]. The parallel lamination of the fine to coarse-grained sandstones indicates a common transition to an upper-flow regime and deposition of planar bed flows in channels or sheet flood deposits [64,68]. The SPL Lithofacies was deposited in a middle alluvial fan area [68,70].

### 5.3.5. Lithofacies GMM1: Massive Matrix Supported Conglomerates

Lithofacies GMM1 comprises matrix supported conglomerates with thicknesses varying between 0.10 to 0.15 m. This lithofacies shows reddish and greyish colors with clast sizes ranging from granules to pebbles (Figure 7e). The matrix supported fabric is mainly composed of medium to coarse sand, which is rich in plagioclase and ferromagnesian minerals. Internally, the matrix-supported conglomerates are unstructured, while the andesitic clasts are sub-rounded.

Matrix supported conglomerates are generally produced by debris flows [74]. Due to the difficulty of transporting gravel clasts, these particles are concentrated at the base of a turbulent flow, forming a dense inertial layer. Lithofacies GMM1 was deposited in a subaerial environment within the upper part of an alluvial fan [68,73].

### 5.3.6. Lithofacies GCM1: Massive Clast Supported Conglomerates

The lithofacies GCM1 includes reddish, clast-supported conglomerate beds with thicknesses ranging from 0.6 to 2 m. The layers show moderate sorting, sharp bases and rounded clasts that range in size from granule to pebbles (2 to 32 mm), with high sphericity. The matrix is composed of fine to very fine particles, without a preferential orientation (Figure 8f). The clasts are dominantly andesites, with minor diorites.

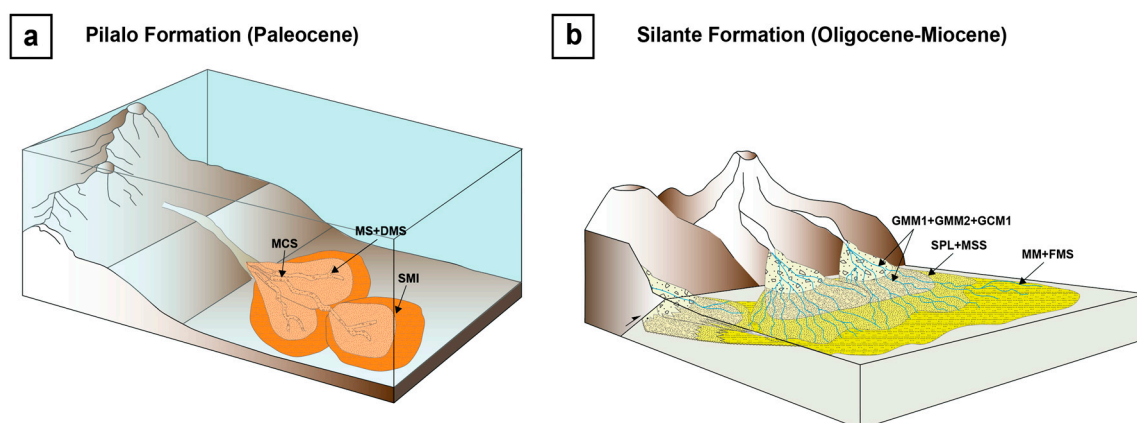


**Figure 8.** Depositional models for the Pilalo and Silante formations. (a) Submarine fan depositional model of the Pilalo Formation, (b) debris flow dominated alluvial fan model of the Silante Formation.

Clast supported conglomerates within alluvial fans are formed when clast-rich debris flows are deposited onto overlying beds that have a high permeability. The fine-grained fraction of the debris flow percolates downwards through the pore spaces of the underlying strata, producing a clast-supported conglomerate [68]. The GCM1 lithofacies infills channels in the upper part of an alluvial fan system [68].

#### 5.3.7. Lithofacies GMM2: Matrix Supported Conglomerates

Lithofacies GMM2 includes poorly sorted dark green conglomerates with clast sizes that vary from granules to blocks, with edges varying from angular to sub-rounded. Most of the larger clasts with sub-rounded to subangular edges are andesites and basaltic andesites (Figure 7g). The smaller clasts with angular edges are similar to lithofacies FMS and MM. The matrix of this lithofacies is composed of fairly well-preserved crystals, with sizes that range from coarse to very coarse sand (0.5 to 2 mm), which is rich in plagioclase, pyroxenes and amphiboles. Inverse grading was observed at the base of the beds.

Poorly sorted and structureless conglomerates with angular clasts may represent the proximal facies of an alluvial fan depositional system [68,75,76], close to the alluvial fan head.

#### 5.4. Depositional Environment of the Pilalo and Silante Formations

The lithofacies association of the Pilalo Formation suggests that the sediments were deposited within a submarine fan (Figure 8a). The distal fan deposits are intercalated with hemipelagic sediments, which corresponds to the transition of a distal depositional lobe to the basin plain [54–57]. The middle fan includes sandy channel deposits [68]. The coarse-grained sediments were deposited by debris flows in channels, which probably formed within the upper part of the fan [61,68]. In addition, the presence of andesitic clasts and abundant mafic minerals suggests a nearby volcanic arc.

Based on the observed lithofacies of the Silante Formation, we suggest that the sedimentary rocks formed in a debris flow dominated alluvial fan (Figure 8b). The upper fan consists of conglomeratic lithofacies deposited by debris flow process [67,68,74–76]. These deposits are mainly exposed in the westernmost part of the Silante Formation. In the Calacalí–Nanegalito section, these coarse deposits occur in greater proportions in the lower part of the stratigraphic column (Figure 5). The middle fan includes reddish sandy channels or sheet flood sediments that were deposited by water-laid processes [64,68–70,72]. The distal alluvial fan and flood plain deposits are represented by interfingering of siltstones and mudstones [65,68,73,75]. These fine-grained deposits are commonly observed in the eastern part of the Calacalí–Nanegalito and Nono–Tandayapa sections (Figure 4).

### 5.5. Provenance Analysis of the Pilalo and Silante Formations

Provenance analyses of clastic deposits of the Pilalo and Silante formations is used to refine the stratigraphic and tectonic interpretation by deciphering shifts in sediment source and source area location. Provenance shifts are associated with the evolution of the sedimentary basins, and hence the tectonic setting [2].

Here, we combine heavy mineral analyses, single grain geochemistry of clinopyroxenes and U-Pb detrital zircon dates. The U-Pb ages of detrital zircons can be used to estimate the maximum depositional age (MDA). Given that these units were deposited proximal to a magmatic arc, it is reasonable to suggest that the zircon U-Pb dates are close approximations of the time of deposition of the sedimentary rocks [77,78].

### 5.6. Heavy Mineral Data

The detrital assemblages of clastic sedimentary rocks reflect the mineralogical composition of the source regions that fed the catchment basin and its depositional history [2,79–82]. In this study, twelve sandstones of the Silante Formation and the underlying Pilalo Formation were selected for heavy mineral analyses (Figure 9). For comparison, the heavy mineral assemblages of three samples from the Campanian–Maastrichtian Yunguilla Formation are shown in Figure 9. Sample locations are presented in Table 1.

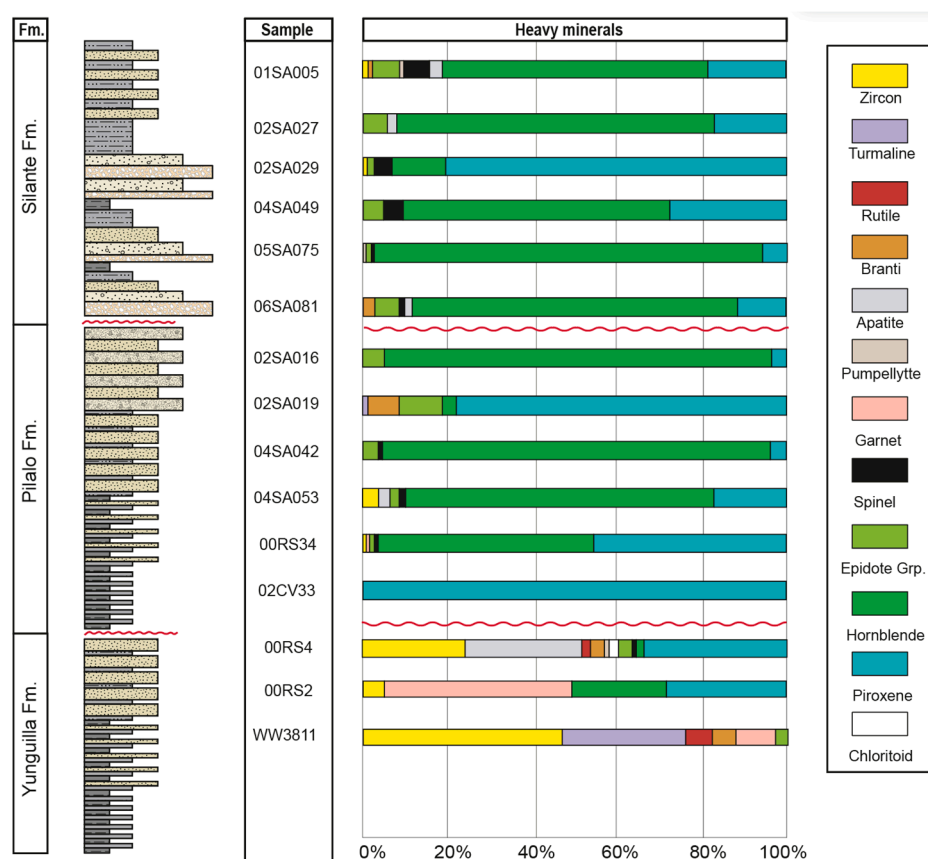


**Figure 9.** Composite stratigraphic column of the Yunguilla, Pilalo and Silante formations and heavy mineral frequencies (right). A clear change is observed in the composition of the Pilalo and Silante formations, which were derived from volcanic sources, whereas Campanian–Maastrichtian sediments of the Yunguilla Formation were shed from granitic and metamorphic sources that formed part of a continental plate, and now constitute the Eastern Cordillera.

All samples from the Pilalo Formation contain a high percentage of pyroxene (modal average of 26%), hornblende (average of 65%) and minerals of the epidote group (average ~4%). These samples yield a null ZTR (zircon-tourmaline-rutile assemblages) index with the exception of rocks 02SA019 and 04SA053, which give a low ZTR index due to a higher percentage of zircons (~3%) and tourmaline.

Samples from the Silante Formation contain a high amount of pyroxene (~27%), hornblende (~64%) and minerals of the epidote group (~3%). In general, samples of the Silante Formation have a very low ZTR index, and no metamorphic accessory minerals have been found. Rocks 01SA005 and 02SA029 contain euhedral zircon crystals (~1%), which are interpreted to have a volcanic origin. The high amounts of pyroxene, hornblende and apatite (~64%) suggests that the source area was strongly dominated by intermediate volcanic rocks [40].

For the Yunguilla Formation, the heavy minerals assemblages of sample WW3311 host a significant ZTR assemblage (82%), with minor amounts of brookite, anatase and titanite (~5%). Garnet and epidote represent ~13%. The heavy mineral in sample 00RS2 include pyroxenes and brown hornblendes (50%) that dominate over smaller amounts of garnet (42%) and zircon (6%). Sample 00RS4 of the Yunguilla Formation contains abundant ZTR group minerals (55%), while pyroxene and hornblende account for ~35%. The heavy minerals assemblages for the Yunguilla Formation suggest that sediments were derived from the erosion of a mixed granitic, metamorphic, and volcanic source.

Overall, the heavy mineral assemblages (Figure 9) reveal a strong volcanic input into the Pilalo and Silante formations, whereas the Yunguilla Formation was predominantly derived from the erosion of granitic rocks and/or metamorphic rocks of the Eastern Cordillera.

### 5.7. Clinopyroxene Single Grain Geochemistry of the Pilalo and Silante Formations

The chemical composition of clinopyroxene is directly related to the chemistry of their host lavas [81,82] and varies according to the magma type, and hence the tectonic setting [81–84]. Beccaluva et al. [84] proposed that the clinopyroxene compositional variability is mostly related to differences in the bulk chemistry of the host magmas, and is only partially due to physical conditions of crystallization, and magmatic fractionation.

We present major element compositions of clinopyroxenes from rocks of the Pilalo and the Silante formations. Samples 00RS34 and 00RS35 of the Pilalo Formation were collected in the Calacalí-Nanegalito road section, and andesite 03CV172 was collected to the north of the Nono locality (Figure 4). Three reddish volcanoclastic sandstones of the Silante Formation were sampled along the Alóag–Santo Domingo road (00RS26), the Otavalo–Selva Alegre road (02CV99), and from the Calacalí–Nanegalito road (02CV56). The full data of major element composition of clinopyroxene is available in the online supplementary material (Table S1).

All analysed clinopyroxenes lack zoning and were optically and chemically homogeneous. Major oxides geochemical data from the analysed clinopyroxenes yields diopsidic to augitic compositions.

To determine the magmatic affinity of the source of the detrital clinopyroxenes we used the discriminatory diagrams of Leterrier et al. [82] (Figure 11). The clinopyroxenes from sandstones of the Silante Formation were derived from a subalkaline volcanic source, although the discriminatory diagram of Al and Ti does not distinguish between a calc-alkaline or tholeiitic composition for these samples (Figure 10). However, the low Al and magnesium numbers (0.62 to 0.65) suggest that the source regions were composed of fractionated rocks, which generally supports a calc-alkaline affinity.

Detrital clinopyroxenes of the Silante Formation plot in the field of subalkaline basalts ( $Ti < 0.025$  apfu), which formed within a subduction zone setting (Figure 11). However, a comparison of Al and Ti does not show a clear distinction between tholeiitic and calc-alkaline affinities. This can be due to the presence of clasts of the Pallatanga Formation and Rio Cala Group, which have a tholeiitic affinity [22].

Clinopyroxene from the Pilalo Formation gave a tholeiitic composition (Figure 11a,c) and probably formed in a subduction zone setting (Figure 11b).

In addition, we used clinopyroxene REE compositions to decipher the geochemical affinity of the magmatic source. The analysed samples include a lava within the Pilaló Formation (03CV172), and two sandstone samples of the Silante Formation (00RS26, and 02CV56).

LREE enrichments (relative to HREE) is regularly found in rocks formed in continental volcanic arcs, whereas a depletion of LREE, and flat REE patterns are more indicative of a primitive island arc, MORB and mantle-plume related, volcanic rocks [85]. In order to determine the composition of the clinopyroxene parent magmas, REE compositions of melts in equilibrium with these minerals were calculated using experimentally derived partition coefficients for clinopyroxenes crystallizing in basaltic rocks [86]. REE values of the analyzed samples were normalized using chondrite values published by Sun and McDonough [87]. The full data of REE composition of clinopyroxene is available in the online supplementary material (Table S2).

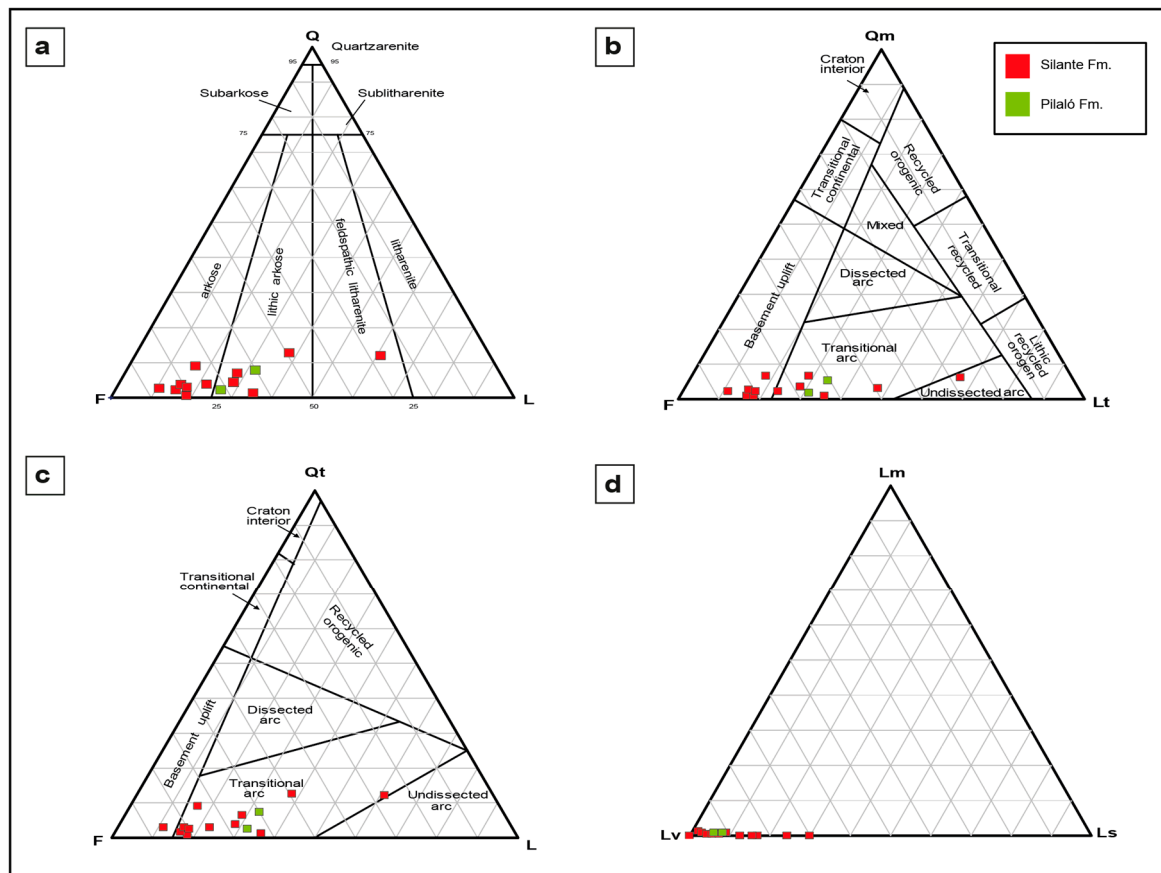


**Figure 10.** Sandstone ternary diagrams for the Pilaló and Silante formations. (a) Ternary diagram with discrimination fields using the terminology of Folk [88]. (b) Ternary discriminatory diagram of monocrystalline quartz (Qm), feldspar (F) and total lithics (Lt) after Dickinson [43]. (c) Ternary discriminatory diagram of quartz (Qt), feldspar (F) and lithics (L) after Dickinson [42]. (d) Ternary discriminatory diagram of metamorphic lithics (Lm), sedimentary lithics (Ls) and volcanic lithics (Lv) after Dickinson [43].

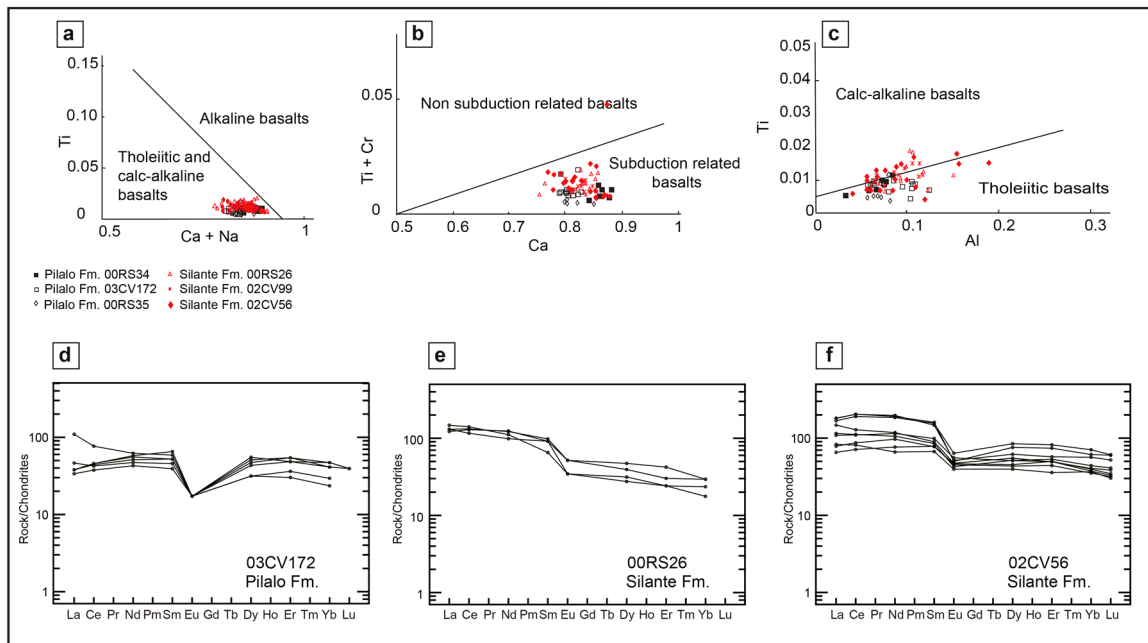


**Figure 11.** Geochemistry of detrital clinopyroxenes from the Silante and Pilalo formations. (a) Ti vs. Ca + Na discriminatory diagram from Leterrier et al. [82]. (b) Ti + Cr vs. Ca discriminatory diagram from Leterrier et al. [82]. (c) Ti vs. Al discriminatory diagram from Leterrier et al. [82]. (d) Chondrite-normalized REE plots of calculated melts in equilibrium with clinopyroxenes of a lava intercalated within the Pilalo Formation (sample 03CV172). (e) Chondrite-normalized REE plots of calculated melts in equilibrium with clinopyroxenes of the Silante Formation (sample 00RS26). (f) Chondrite-normalized REE plots of calculated melts in equilibrium with clinopyroxenes of the Silante Formation (sample 02CV56). Chondrite normalizing values after Sun and McDonough [87].

For sample 03CV172, the calculated melt in equilibrium with the clinopyroxenes yields a REE chondrite normalized profile that is generally flat (Figure 11), and the  $(La/Yb)_N$  ratio is  $\sim 1$ , suggesting a primitive nature of the magmas in which the clinopyroxene crystallized. The calculated melt in equilibrium with clinopyroxenes extracted from sandstones of the Silante Fm. shows LREE enrichments up to 100 times chondritic values (Figure 11e,f). The  $(La/Yb)_N$  ratios vary between 5.32 (00RS26) and 2.58 (02CV56), which are typical for arc rocks [86].

Summarizing, clinopyroxenes of the Silante Formation are compositionally distinct from clinopyroxenes extracted from the Pilalo Formation. The enrichment of LREE and low Ti values of detrital clinopyroxenes of the Silante Formation (Figure 11e,f) are probably the result of dehydration of subducted oceanic crust, which released fluids that have low concentrations of Ti [82] and high concentrations of REE. The LREE enrichment, together with the low to medium concentrations of Al suggests that the volcanic source rocks of the Silante Formation is more evolved than the volcanic source of the Pilalo Formation.

### 5.8. QFL Analysis (Quartz-Feldspar-Lithic Fragments)

Fourteen petrographic thin sections of sandstones of the Pilalo and Silante formations were analysed for modal sandstone composition. The relative proportions of detrital grains, including feldspar (F), quartz (Q), and lithic fragments (L), combined with grain size, provide a formal name for the sedimentary rock [41,88], and constrain the tectonic settings of the source regions [42]. According to the QFL classification diagram of Folk [88], sandstones of the Silante Formation are classified as arkoses to lithic arkoses, whereas samples of the Pilalo Formation are lithic arkoses (Figure 10a).

In the Qm-F-Lt discriminatory diagram (Figure 10b), samples of the Pilalo Formation plot in the transitional arc field. Sedimentary rocks of the Silante Formation contain a greater amount of feldspar

grains and volcanic lithic fragments, and these rocks cluster in the transitional arc and basement fields (Figure 10b,c). The LmLvLs diagrams for both formations reveal high contents of volcanic lithics and small amounts of sedimentary lithoclasts (Figure 10d).

The relative proportions of quartz, feldspar, and lithic fragments in the Pilalo and Silante formations reveal provenance shifts that can be related to changes in their sediment source areas. Overall, the results imply that clastic sedimentary rocks in the Silante and Pilalo basins were supplied from the erosion of volcanic arcs.

### 5.9. U-Pb Ages of the Silante Formation

U-Pb zircon dates were obtained from detrital zircons from sedimentary rocks of the Silante Formation, including rocks 02SA027, 02SA028, 02SA029 and JL17002 (Table 1, Figure 2). We also present zircon U-Pb analyses of quartz diorite (JL17003), which intrudes sedimentary rocks of the Silante Formation to the southwest of Quito, along the Quito–Santo Domingo road (Figure 4). The full LA-ICP-MS U-Pb zircon age data is available in the online supplementary material (Table S3).

Sandstone 02SA027 shows a unimodal peak at ~25 Ma (Figure 12a), with an MDA age of  $25.017 \pm 0.07$  Ma ( $2\sigma$ ) (Oligocene). A single detrital zircon with an age of  $553.9 \pm 6.46$  Ma was measured. This zircon can be derived from the Brazilian belt (500–700 Ma), formed during the assembly of Gondwana [41,89]. Furthermore, it is a common population in detrital zircons obtained within the Eocene Angamarca Group of western Ecuador [2]. In sample 02SA028 a unimodal peak (Figure 12b), with an MDA age of  $24.64 \pm 0.17$  Ma ( $2\sigma$ ) was obtained.

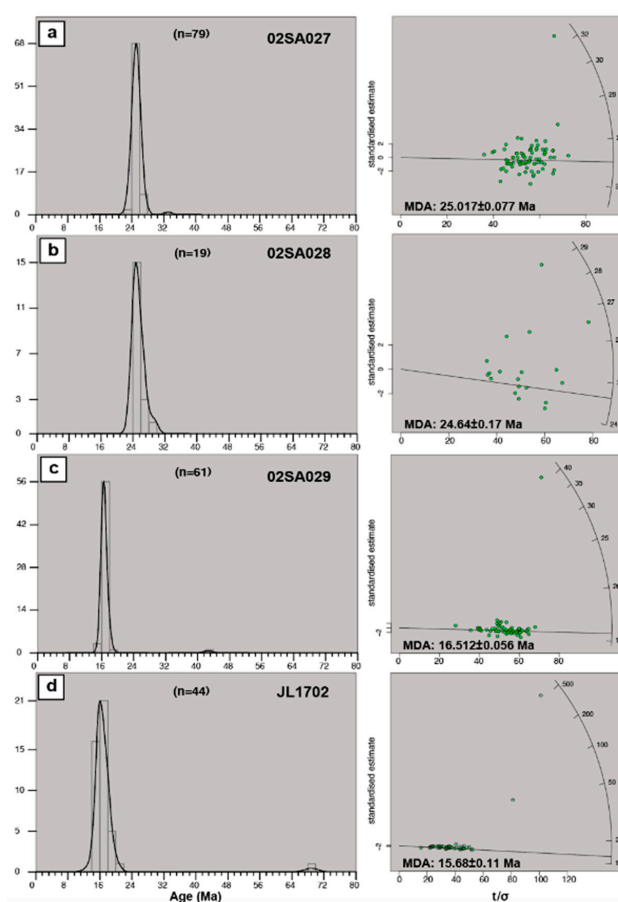


**Figure 12.** Frequency and probability density plots of detrital zircon U-Pb ages (left) and maximum depositional ages (MDA, right) from samples of the Silante Formation (a) sample 02SA027; (b) 02SA028; (c) 02SA029; (d) JL1702. The  $t/\sigma$  ratio on X-axis indicates the precision.

Sample 02SA029 also shows a unimodal peak at ~16 Ma (early Miocene). The MDA age obtained (Figure 12c) is  $16.51 \pm 0.056$  Ma ( $2\sigma$ ). A single detrital zircon revealed an age of  $42.6 \pm 0.6$  Ma which can be correlated with the Macuchi volcanism of the Western Cordillera of Ecuador, dated at  $42.62 \pm 1.3$  Ma with the U-Pb zircon dating method [90].

Sample JL17002 revealed a unimodal peak at ~16 Ma (early Miocene), and an MDA of  $15.68 \pm 0.11$  (Figure 12d). In addition, two detrital zircons with ages of  $68.9 \pm 1.7$  Ma, and  $67.8 \pm 2.6$  Ma were detected. These Maastrichtian zircons are probably derived from the erosion of the Pilalo and Tandapi rocks.

Quartz diorite JL17003 intrudes sedimentary rocks of the Silante Formation and is exposed along the Alóag–Santo Domingo road section (Figure 2). The sample yields a weighted mean zircon U-Pb (LA-ICPMS) age of  $10.31 \pm 0.27$  Ma (Figure 13), interpreted as crystallization age.

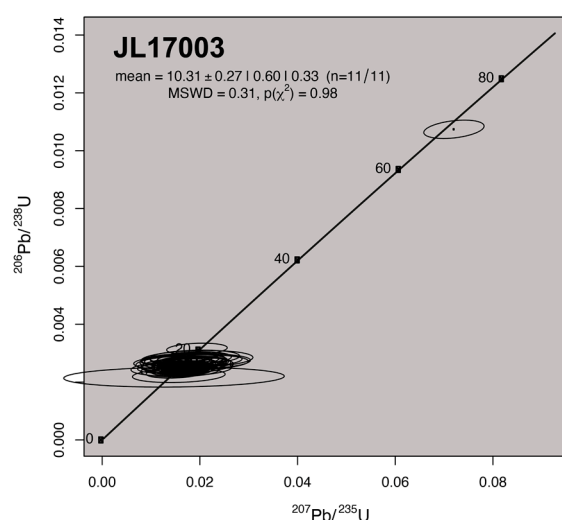


**Figure 13.** U-Pb LA-ICPMS zircon age of a quartz diorite intruding the Silante Formation (sample JL17003), plotted on a concordia diagram. Errors are given at the  $2\sigma$  level.

## 6. Discussion: Paleogeographic and Paleotectonic Model

Sedimentological information and provenance analysis in the study area of the Western Cordillera of Ecuador show that turbidite sedimentation prevailed during the Paleocene, with the deposition of the Pilalo Formation. The main sedimentary source was a tholeiitic volcanic arc that can be related to the Tandapi arc reported by Vallejo et al. [2], which formed on top of an oceanic plateau basement. Therefore, the Paleocene sedimentary rocks described in this study do not correlate with the Campanian to Maastrichtian Yunguilla Formation. The Yunguilla Formation was also deposited in a submarine fan system, although provenance analysis indicates the sediments were eroded from a continental crust block, which is probably currently represented by the Eastern Cordillera.

The chronostratigraphic and sedimentological data suggest that the Silante Formation was deposited during the late Oligocene to Miocene period (~25–16 Ma) within a debris flow dominated alluvial fan system. The Silante Formation formed after a period of major rock uplift and erosion of the Western Cordillera. The Paleocene to Eocene submarine fan deposits of the Angamarca Group were probably partly eroded in the study area before deposition of the Silante Formation, and they are exposed several kilometers to the north and south of the study area (Figure 2).

Single grain geochemistry and petrographic analysis show that the Silante Formation received detrital material from a coeval calc-alkaline volcanic arc, which was presumably the San Juan de Lachas continental arc located in the Western Cordillera, to the northwest of the current exposures of the Silante Formation (Figure 2). A western location for the source of the Silante Formation is also suggested by the abundance of coarse-grained deposits to the west of the studied sections (Figure 4).

Petrographic analysis and detrital U-Pb zircon ages reveal a minor contribution of sediment to the Silante Formation from basement rocks, along with material from the erosion of the underlying Pilalo Formation, and the Eocene Macuchi submarine arc. Clinopyroxene compositions show that these were derived from calc-alkaline rocks, with a minor contribution from a tholeiitic volcanic source. The latter is consistent with the presence of clasts from the Pallatanga and Rio Cala volcanic rocks, suggesting the that basement was unroofed during sedimentation.

The Miocene period in Ecuador is generally characterized by the formation of large alluvial fan systems, including the Biblian alluvial fan in southern Ecuador in an intramontane setting [31]. The Arajuno Formation in the back-arc foreland basin also represents an alluvial fan system sourced from the Andes [91] and has been dated at ~17–13 Ma using U-Pb ages of detrital zircons [28].

(U-Th)/He and  $^{40}\text{Ar}/^{39}\text{Ar}$  fission track data from the Andes of Ecuador [92] reveals rapid cooling and exhumation during 25–18 Ma, which correlates with a change in the vector of the subducting plate from ESE to E at 25 Ma, as a result of the breakup of the Farallon Plate [92–94], forming the Nazca and Cocos plates. Compressional events have also been dated between 25 and 15 Ma in the Andes of Bolivia and Peru [92–97]. Clearly, major plate rearrangements at 25 Ma affected the South American Plate to the north and south of the Huancabamba Deflection [92]. In addition, middle to late Miocene broadening of arc magmatism in the Eastern and Western Cordilleras [12,28] accounts for appearance of syndepositional age signatures within the Western Cordillera and the back-arc region [27,28].

Palinspastic constraints based on the results of this study are presented in Figure 14. During the Paleocene, the Pilalo Formation was deposited in a submarine fan depositional environment, with sediments sourced from the erosion of the tholeiitic Tandapi volcanic arc (Figure 14a). Igneous rocks associated with this volcanic arc include the Tandapi volcanic and subvolcanic rocks that are exposed in the study area with crystallization ages of ~65 to 61 Ma [11].

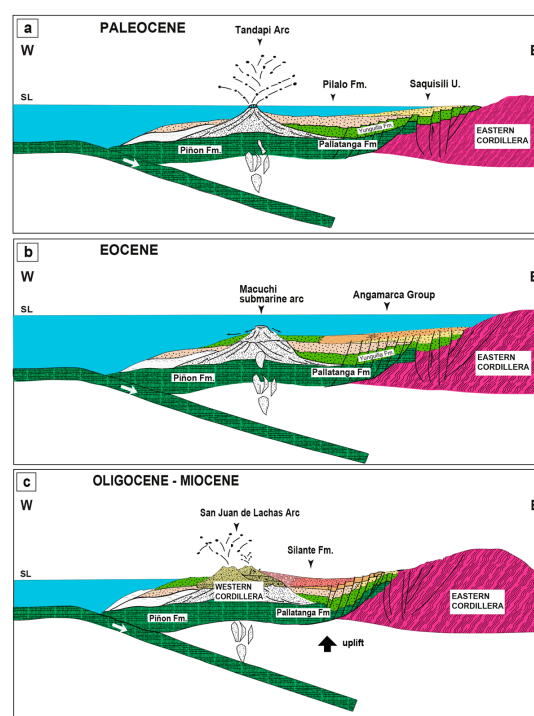


**Figure 14.** Tectonic evolution of the Western Cordillera of Ecuador during the Cenozoic. The initial uplift started at the end of the Cretaceous. (a) Paleocene paleogeography of the Pilalo Formation submarine fan with the coeval Tandapi arc; (b) Eocene Macuchi submarine arc and sedimentation of the Angamarca Group; (c) during the Oligocene to Middle Miocene there is a rapid uplift of the Eastern and Western Cordilleras, and the deposition of the Silante Formation in an intramontane basin setting. SL: sea level.

Submarine sedimentation continued during most of the Eocene period with the submarine fan of the Angamarca Group [22], depositing sediments that were mainly sourced from the Eastern Cordillera (Figure 14b).

A change from submarine to subaerial sedimentation occurred in broad areas of the Western Cordillera during the Oligocene [2], which coincides with a rapid rock uplift and exhumation of the Eastern and Western cordilleras [2]. The San Juan de Lachas continental arc was active during this period (Figure 14c) and extended into the Miocene [18], and supplied sediments to the Silante alluvial fan, which was deposited in an intramontane basin setting (Figure 14c).

The last deformation event recorded in rocks of the Silante Formation postdates the intrusion of the quartz diorite dated in this study, which yields a U-Pb crystallization age of  $10.31 \pm 0.27$  Ma. This deformation phase may coincide with a latest Miocene-Pliocene phase of deformation, prior to the deposition of Quaternary volcanic ash of the Cangahua Formation [2,92,98].

## 7. Conclusions

Stratigraphic and sedimentological analyses of the Pilalo Formation, which is in fault contact with the Silante Formation, indicate that the sediments were deposited in the distal parts of a submarine fan. The Pilalo Formation was coeval with the latest Maastrichtian to Paleocene Tandapi volcanic arc, which formed on top of the accreted terranes of western Ecuador.

Radiometric dating indicates the Silante Formation in the study region was deposited during the late Oligocene to middle Miocene, subsequent to local erosion of the Eocene Angamarca Group.

Stratigraphic and sedimentologic analyses of the Silante Formation show that the sediments were deposited in a continental alluvial fan system that was dominated by debris flow processes and formed in an intramontane setting. Petrographic and provenance analyses of the same sediments suggest they were derived from the erosion of an andesitic continental volcanic arc, which was probably the Oligocene San Juan de Lachas arc.

Thermochronological data and regional correlations suggest that deposition of the Silante Formation was coeval with regional rock uplift and exhumation of the Andean margin, which gave rise to alluvial fans in intermontane and back-arc domains. This phase of regional deformation is temporally correlated with a phase of major plate reorganization during the breakup of the Farallon Plate.

**Supplementary Materials:** The following are available online at <http://www.mdpi.com/2075-163X/10/10/929/s1>, LA-ICP-MS U-Pb zircon age data and clinopyroxene geochemistry. Table S1. Chemical composition and structural formula of clinopyroxene phenocrysts. Table S2. REE elements composition of clinopyroxenes from the Western Cordillera. Table S3. LA-ICP-MS U-Pb dating data of detrital zircons sample.

**Author Contributions:** Conceptualization, C.V., S.A., V.E. and C.R.; methodology, C.V. and J.L.H.; software, V.E.; validation, R.A.S. and W.W.; formal analysis, P.V. All authors have read and agreed to the published version of the manuscript.

**Funding:** This work is part of the EPN project PIS-18-04. The authors would like to express their gratitude to the company Geostrat S.A. Ecuador for the partial financial support of this project.

**Acknowledgments:** We thank Bernardo Beate and Brian K. Horton for fruitful discussions about the geology of Ecuador and the Western Cordillera. Fieldwork benefited from the knowledge of Efrain Montenegro, Michel Toro and Arturo Egüez.

**Conflicts of Interest:** The authors declare no conflict of interest.

## References

1. Luzieux, L.D.; Heller, F.; Spikings, R.; Vallejo, C.F.; Winkler, W. Origin and Cretaceous tectonic history of the coastal Ecuadorian forearc between 1° N and 3° S: Paleomagnetic, radiometric and fossil evidence. *Earth Planet. Sci. Lett.* **2006**, *249*, 400–414. [[CrossRef](#)]
2. Vallejo, C.; Spikings, R.A.; Horton, B.K.; Luzieux, L.; Romero, C.; Winkler, W. Late Cretaceous to Miocene stratigraphy and provenance of the coastal forearc and Western Cordillera of Ecuador: Evidence for accretion of a single oceanic plateau fragment. In *Andean Tectonics*, 1st ed.; Horton, B., Folguera, A., Eds.; Elsevier: Amsterdam, The Netherlands, 2019; pp. 209–236.

3. Feininger, T.; Bristow, C.R. Cretaceous and Palaeogene geologic history of Coastal Ecuador. *Geol. Rundsch.* **1980**, *69*, 40–44. [[CrossRef](#)]
4. Chiaradia, M. Adakite-like magmas from fractional crystallization and melting-assimilation of mafic lower crust (Eocene Macuchi arc, Western Cordillera, Ecuador). *Chem. Geol.* **2009**, *265*, 468–487. [[CrossRef](#)]
5. Kehrer, W.; Van Der Kaaden, G. Notes on the geology of Ecuador, with special reference to the Western Cordillera. *Geol. Jahrb.* **1979**, *35*, 5–57.
6. Henderson, W.G. Cretaceous to Eocene volcanic arc activity in the Andes of northern Ecuador. *J. Geol. Soc. Lond.* **1979**, *136*, 73–78.
7. Egüez, A. Evolution Cenozoique de la Cordillere Occidentale Septentrionale d'Equateur (0°15' S–01°10' S) les Mineralisations Associeees. Ph.D. Thesis, University of Pittsburgh Medical Center, Paris, France, 1986.
8. Kerr, A.C.; Aspden, J.A.; Tarney, J.; Pilatasig, L.F. The nature and provenance of accreted oceanic Blocks in western Ecuador: Geochemical and tectonic constraints. *J. Geol. Soc.* **2002**, *159*, 577–594. [[CrossRef](#)]
9. Jaillard, E.; Ordoñez, M.; Suarez, J.; Toro, J.; Iza, D.; Lugo, W. Stratigraphy of the late Cretaceous Paleogene deposits of the cordillera occidental of central Ecuador: Geodynamic implications. *J. S. Am. Earth Sci.* **2004**, *17*, 49–58. [[CrossRef](#)]
10. Spikings, R.A.; Winkler, W.; Hughes, R.A.; Handler, R. Thermochronology of Allochthonous Blocks in Ecuador: Unraveling the accretionary and post-accretionary history of the Northern Andes. *Tectonophysics* **2005**, *399*, 195–220. [[CrossRef](#)]
11. Vallejo, C.; Winkler, W.; Spikings, R.A.; Luzieux, L.; Heller, F.; Bussy, F. Mode and timing of terrane accretion in the forearc of the Andes in Ecuador. In *Backbone of the Americas: Shallow Subduction, Plateau Uplift, and Ridge and Terrane Collision*, 1st ed.; Kay, S., Ramos, V., Dickinson, W., Eds.; Geological Society of America Memoirs: Boulder, CO, USA, 2009; Volume 204, pp. 197–216.
12. Schütte, P.; Chiaradia, M.; Beate, B. Geodynamic controls on Tertiary arc magmatism in Ecuador: Constraints from U–Pb zircon geochronology of Oligocene–Miocene intrusions and regional age distribution trends. *Tectonophysics* **2010**, *489*, 159–176. [[CrossRef](#)]
13. Beate, B.; Monzier, M.; Spikings, R.; Cotton, J.; Silva, J.; Bourdon, E.; Eissen, J.P. Mio-Pliocene adakite generation related to flat subduction in southern Ecuador: The Quimsacocha volcanic center. *Earth Planet. Sci. Lett.* **2001**, *192*, 561–570. [[CrossRef](#)]
14. Baldock, J. *Geology of Ecuador: Explanatory Bulletin of the National Geological Map of the Republic of Ecuador*, 1st ed.; DGGM: Quito, Ecuador, 1982; p. 70.
15. Herrera, J.L. La-ICP-MS Zircon U-Pb Geochronology on the Ecuadorian Andes and Forearc, Constraints in Their Cretaceous–Paleogene Evolution: SILANTE Formation, CATACocha Unit, CAÑAVERAL Formation. Master's Thesis, University College, London, UK, 2018.
16. Wallrabbe-Adams, H.J. Petrology and geotectonic development of the Western Ecuadorian Andes: The Basic Igneous Complex. *Tectonophysics* **1990**, *185*, 163–182. [[CrossRef](#)]
17. Hughes, R.; Bermudez, R. *Geology of the Cordillera Occidental of Ecuador between 0°00' and 1°00' S. Proyecto de Desarrollo Minero y Control Ambiental, Programa de Información Cartográfica y Geológica; Report Number 4*, 1st ed.; CODIGEM-BGS: Quito, Ecuador, 1997; p. 75.
18. Boland, M.P.; Pilatasig, L.F.; Ibadango, C.E.; McCourt, W.J.; Aspden, J.A.; Hughes, R.A.; Beate, B. *Geology of the Western Cordillera between 0°–1°N, Proyecto de Desarrollo Minero y Control Ambiental, Programa de Informacion cartografica y Geológica, Informe No. 10*; CODIGEM-BGS: Quito, Ecuador, 2000; p. 72.
19. Jaillard, E.; Ordoñez, M.; Benitez, S.; Berrones, G.; Jimenez, N.; Montenegro, G.; Zambrano, I. Basin Development in an Accretionary, Oceanic-floored Fore-Arc Setting: Southern Coastal Ecuador During Late Cretaceous–Late Eocene time. *AAPG Mem.* **1995**, *62*, 615–631.
20. Winkler, W.; Villagómez, D.; Spikings, R.; Abegglen, P.; Tobler, S.; Egüez, A. The Chota basin and its significance for the inception and tectonic setting of the Inter-Andean Depression in Ecuador. *J. S. Am. Earth Sci.* **2005**, *19*, 5–19. [[CrossRef](#)]
21. Cotteccia, V.; Zezza, F. The Eocene basement of the inter-Andean corridor in the Latacunga Ambato trough (Ecuador). *Geol. Appl. Idrogeol.* **1969**, *4*, 43–46.
22. Vallejo, C.F. Evolution of the Western Cordillera in the Andes of Ecuador (Late Cretaceous Paleogene). Ph.D. Thesis, ETH Zürich, Zürich, Switzerland, 2007.
23. Hughes, R.A.; Pilatasig, L.F. Cretaceous and Tertiary Block accretion in the Cordillera Occidental of the Andes of Ecuador. *Tectonophysics* **2002**, *345*, 29–48. [[CrossRef](#)]

24. Litherland, M.; Aspden, J.; Jemielita, R.A. *The Metamorphic Belts of Ecuador. Overseas Memoir 11*; BGS: Keyworth, UK, 1994; p. 147.
25. Spikings, R.; Cochrane, R.; Villagomez, D.; Van der Lelij, R.; Vallejo, C.; Winkler, W.; Beate, B. The geological history of northwestern South America: From Pangaea to the early collision of the Caribbean Large Igneous Province (290–75 Ma). *Gond. Res.* **2015**, *27*, 95–139. [[CrossRef](#)]
26. Ruiz, G.M.H.; Seward, D.; Winkler, W. Detrital thermochronology—A new perspective on hinterland tectonics, an example from the Andean Amazon Basin, Ecuador. *Basin Res.* **2004**, *16*, 413–430. [[CrossRef](#)]
27. Gombojav, N.; Winkler, W. Recycling of Proterozoic crust in the Andean Amazon foreland of Ecuador: Implications for orogenic development of the northern Andes: Multiple recycling of Proterozoic crust in the northern Andes. *Terra Nova* **2008**, *20*, 22–31. [[CrossRef](#)]
28. Gutiérrez, E.G.; Horton, B.K.; Vallejo, C.; Jackson, L.J.; George, S.W. Provenance and geochronological insights into Late Cretaceous–Cenozoic foreland basin development in the Subandean Zone and Oriente Basin of Ecuador. In *Andean Tectonics*, 1st ed.; Horton, B., Folguera, A., Eds.; Elsevier: Amsterdam, The Netherlands, 2019; pp. 237–268. [[CrossRef](#)]
29. Vallejo, C.F.; Spikings, R.A.; Winkler, W.; Luzieux, L.; Chew, D.; Page, L. The early interaction between the Caribbean Plateau and the NW South American Plate. *Terra Nova* **2006**, *18*, 264–269. [[CrossRef](#)]
30. Van Thournot, F.; Hertogen, J.; Quevedo, L. Allochthonous Blocks in northern Ecuador. *Tectonophysics* **1992**, *205*, 205–222.
31. Hungerbühler, D.; Steinmann, M.; Winkler, W.; Seward, D.; Egüez, A.; Peterson, D.E.; Hammer, C. Neogene stratigraphy and Andean geodynamics of southern Ecuador. *Earth Sci. Rev.* **2002**, *57*, 75–124. [[CrossRef](#)]
32. Sinton, C.W.; Duncan, R.A.; Storey, M.; Lewis, J.; Estrada, J.J. An oceanic flood basalts province within the Caribbean plate. *Earth Planet. Sci. Lett.* **1998**, *155*, 221–235. [[CrossRef](#)]
33. Mamberti, M.; Lapierre, H.; Bosch, D.; Jaillard, E.; Hernandez, J.; Polve, M. The Early Cretaceous San Juan Plutonic Suite, Ecuador: A magma chamber in an oceanic plateau? *Can. J. Earth Sci.* **2004**, *41*, 1237–1258. [[CrossRef](#)]
34. Thalmann, H.E. Micropaleontology of upper Cretaceous and Paleocene in western Ecuador. *AAPG Bull.* **1946**, *30*, 337–347.
35. Cosma, L.; Lapierre, H.; Jaillard, E.; Laubacher, G.; Bosch, D.; Desmet, A.; Mamberti, M.; Gabriele, P. Petrographie et géochimie des unités magmatiques de la Cordillère Occidentale d'Équateur (0°30' S): Implications tectoniques. *Bull. Soc. Géol. Fr.* **1998**, *169*, 739–751.
36. Egüez, A.; Bourgeois, J. La Formación Apagua, edad y posición estructural en la Cordillera Occidental del Ecuador. In *Cuarto Congreso Ecuatoriano de Geología Minas y Petróleos*; Escuela Politécnica Nacional: Quito, Ecuador, 1986; pp. 161–178.
37. Savoyat, F.; Vernet, R.; Sigal, J.; Mosquera, C.; Granja, J.; Guevara, G. *Formaciones Sedimentarias de la Sierra Tectónica Andina del Ecuador*; Servicio Nacional de Geología y Minería—Institut Français du Pétrole; 1970; unpublished report.
38. Van Thournout, F. Stratigraphy, Magmatism and Tectonism in the Ecuadorian Northwestern Cordillera: Metallogenic and Geodynamic Implications. Ph.D. Thesis, Katholieke Universiteit Leuven, Leuven, Belgium, 1991.
39. Cohen, K.M.; Finney, S.C.; Gibbard, P.L.; Fan, J. The ICS International Chronostratigraphic Chart. *Episodes* **2013**, *36*, 199–204. [[CrossRef](#)] [[PubMed](#)]
40. Mange, M.; Maurer, H. *Heavy Minerals in Colour*, 1st ed.; Chapman and Hall: London, UK, 1992; p. 147.
41. Valarezo, M.; Vallejo, C.; Horton, B.K.; Gaibor, J.; Esteban, J.; Jackson, L.J.; Carrasco, H.; Winkler, W.; Bernal, C.; Beate, B. Sedimentological and provenance analysis of the Río Playas stratigraphic section: Implications for the evolution of the Alamor-Lancones Basin of southern Ecuador and northern Peru. *J. S. Am. Earth Sci.* **2019**, *94*, 1–18. [[CrossRef](#)]
42. Dickinson, W.R.; Suczek, C.A. Plate tectonics and sandstone compositions. *AAPG Bull.* **1979**, *63*, 2164–2182.
43. Dickinson, W.R. Interpreting provenance relations from detrital modes of sandstones. In *Provenance of Arenites*, 1st ed.; Zuffa, G., Ed.; Reidel Publishing Company: Dordrecht, The Netherlands, 1985; pp. 331–361.
44. Gazzi, P. Le arenarie del flysch sopracretaceo dell'Appennino modenese; correlazioni con il flysch di Monghidoro. *Miner. Petrogr. Acta* **1966**, *12*, 69–97.
45. Dickinson, W.R. Interpreting detrital modes of graywacke and arkose. *J. Sed. Petrol.* **1970**, *40*, 695–707.

46. Dickinson, W.R.; Beard, L.S.; Brackenridge, G.R.; Erjavec, J.L.; Ferguson, R.C.; Inman, K.F.; Knepp, R.A.; Lindenberg, F.A.; Ryberg, P.T. Provenance of North American Phanerozoic sandstones in relation to tectonic setting. *Geol. Soc. Am. Bull.* **1983**, *94*, 222–235. [[CrossRef](#)]
47. Sláma, J.; Kosler, J.; Condon, D.; Crowley, J.; Gerdes, A.; Hanchar, J.; Horstwood, M.; Morris, G.; Nasdala, L.; Norberg, N.; et al. Plesovice zircon—A new natural reference material for U-Pb and Hf isotopic microanalysis. *Chem. Geol.* **2008**, *249*, 1–35. [[CrossRef](#)]
48. Jochum, K.; Weis, U.; Stoll, B.; Kuzmin, D.; Yang, Q.; Raczek, I.; Jacob, D.; Stracke, A.; Birbaum, K.; Frick, D.; et al. Determination of Reference Values for NIST SRM 610617 Glasses Following ISO Guidelines. *Geostand. Geoanal. Res.* **2011**, *35*, 397–425. [[CrossRef](#)]
49. Wiedenbeck, M.; Hanchar, J.M.; Peck, W.H.; Sylvester, P.; Valley, J.; Whitehouse, M.; Kronz, A.; Morishita, Y.; Nasdala, L.; Fiebig, J.; et al. Further characterisation of the 91500 zircon crystal. *Geostand. Geoanal. Res.* **2004**, *28*, 9–39. [[CrossRef](#)]
50. Vermeesch, P. IsoplotR: A free and open toolbox for geochronology. *Geos. Front.* **2018**, *9*, 1479–1493. [[CrossRef](#)]
51. Galbraith, R.F. *Statistics for Fission Track Analysis*; Chapman and Hall/CRC: Boca Raton, FL, USA, 2005; p. 224.
52. Vermeesch, P. RadialPlotter: A Java application for fission track, luminescence and other radial plots. *Radiat. Meas.* **2009**, *44*, 409–410. [[CrossRef](#)]
53. Galbraith, R. Graphical display of estimates having differing standard errors. *Tectonometrics* **1988**, *30*, 271–281. [[CrossRef](#)]
54. Lowe, D.R. Sediment gravity flows: II. Depositional models with special reference to the deposits of high-density turbidity currents. *J. Sediment. Petrol.* **1982**, *52*, 279–297.
55. Tucker, M.E. *Sedimentology Rocks in the Field*, 3rd ed.; Wiley: England, UK, 2003; pp. 83–158.
56. Shanmugam, G. The Bouma Sequence and the turbidite mind set. *Earth Sci. Rev.* **1997**, *42*, 201–229. [[CrossRef](#)]
57. Shanmugam, G.; Shrivastava, S.K.; Das, B. Sandy Debrisites and Tidalites of Pliocene Reservoir Sands in Upper-Slope Canyon Environments, Offshore Krishna-Godavari Basin (India): Implications. *J. Sediment. Res.* **2009**, *79*, 736–756. [[CrossRef](#)]
58. Postma, G. Classification for sediment gravity-flow deposits based on flow conditions during sedimentation. *Geology* **1986**, *4*, 291–294. [[CrossRef](#)]
59. Shanmugam, G. Glossary: A supplement to “Submarine fans: A critical retrospective (1950–2015)”. *J. Palaeogeogr.* **2016**, *5*, 1–20.
60. Shanmugam, G. 50 years of the turbidite paradigm (1950s–1990s): Deepwater processes and facies models—A critical perspective. *Mar. Pet. Geol.* **2000**, *17*, 285–342. [[CrossRef](#)]
61. Song, S.R.; Lo, H.J. Lithofacies of volcanic rocks in the central Coastal Range, eastern Taiwan: Implications for island arc evolution. *J. Asian Earth Sci.* **2002**, *21*, 23–38. [[CrossRef](#)]
62. Sohn, Y.K. Depositional processes of submarine debris flows in the Miocene fan deltas, Pohang Basin, SE Korea with special reference to flow transformation. *J. Sediment. Res.* **2000**, *70*, 491–503. [[CrossRef](#)]
63. Hughes, D.A.; Lewin, J. A small-scale flood plain. *Sedimentology* **1982**, *29*, 891–895. [[CrossRef](#)]
64. Gao, L.; Wang, X.; Yi, S.; Vandenberghe, J.; Gibling, M.; Lu, H. Episodic Sedimentary Evolution of an Alluvial Fan (Huangshui Catchment, NE Tibetan Plateau). *Quaternary* **2018**, *1*, 16. [[CrossRef](#)]
65. Heward, A. Alluvial fan sequence and megasequence model: With examples from Westphalian D-Stephanian B coalfields, Northern Spain. In *Fluvial Sedimentology*, 1st ed.; Miall, A.D., Ed.; Dallas Geological Society: Dallas, TX, USA, 1977; pp. 669–702.
66. Nichols, G.J.; Fisher, J.A. Processes, facies and architecture of fluvial distributary system deposits. *Sediment. Geol.* **2007**, *195*, 75–90. [[CrossRef](#)]
67. Sohn, Y.K.; Rhee, C.W.; Kim, B.C. Debris Flow and Hyperconcentrated Flood Flow Deposits in an Alluvial Fan, Northwestern Part of the Cretaceous Yongdong Basin, Central Korea. *J. Geol.* **1999**, *107*, 111–132. [[CrossRef](#)]
68. Reineck, H.; Singh, I. *Depositional Sedimentary Environments*; Springer: New York, NY, USA, 1980; p. 549.
69. Mack, G.H.; Leeder, M.R. Climatic and tectonic controls on alluvial-fan and axial- fluvial sedimentation in the Plio Pleistocene Palomas half graben, southern Rio Grande rift. *J. Sediment. Res.* **1999**, *69*, 635–652. [[CrossRef](#)]
70. Bourquin, S.; Rigollet, C.; Bourges, P. High-resolution sequence stratigraphy of an alluvial fan delta environment: Stratigraphic and geodynamic implications. An example from the Keuper Chaunoy Sandstones, Paris Basin. *Sediment. Geol.* **1998**, *121*, 207–237. [[CrossRef](#)]

71. Li, S.; He, H.; Hao, R.; Chen, H.; Bie, H.; Liu, P. Depositional regimes and reservoir architecture characterization of alluvial fans of Karamay oilfield in Junggar basin, Western China. *J. Petr. Sci. Eng.* **2020**, *186*, 1–15. [[CrossRef](#)]
72. Van Houten, F.B. Iron and clay in tropical savanna alluvium: A contribution to the origin of red beds. *Bull. Geol. Soc. Am.* **1972**, *83*, 2761–2772. [[CrossRef](#)]
73. Leleu, S.; Ghienne, J.F.; Manatschal, G. Upper Cretaceous-Palaeocene basin-margin alluvial fans documenting interaction between tectonic and environmental processes (Provence, SE France). *Geol. Soc. Lond. Spec. Publ.* **2005**, *251*, 217–239. [[CrossRef](#)]
74. Neves, M.A.; Morales, N.; Saad, A.R. Facies analysis of tertiary alluvial fan deposits in the Jundiá region, São Paulo, southeastern Brazil. *J. S. Am. Earth Sci.* **2005**, *19*, 513–524. [[CrossRef](#)]
75. Nichols, G. *Sedimentology and Stratigraphy*, 2nd ed.; Wiley-Blackwell: Hoboken, NJ, USA, 2009; pp. 129–150.
76. Ferrando, S.; Bernoulli, D.; Compagnoni, R. The Canavese zone (internal Western Alps): A distal margin of Adria. *Schweizerische Mineralogische und Petrographische Mitteilungen* **2004**, *84*, 237–256.
77. Perez, N.D.; Horton, B.K. Oligocene-Miocene deformational and depositional history of the Andean hinterland basin in the Northern Altiplano Plateau, Southern Peru. *Tectonics* **2014**, *33*, 1819–1847. [[CrossRef](#)]
78. Horton, B.K.; Anderson, V.J.; Caballero, V.; Saylor, J.E.; Nie, J.; Parra, M.; Mora, A. Application of detrital zircon U-Pb geochronology to surface and subsurface correlations of provenance, paleodrainage, and tectonics of the middle Magdalena Valley basin of Colombia. *Geosphere* **2015**, *11*, 1790–1811. [[CrossRef](#)]
79. Morton, A.C.; Hallsworth, C.R. Identifying provenance-specific features of detrital heavy mineral assemblages in sandstones. *Sediment. Geol.* **1994**, *90*, 241–256. [[CrossRef](#)]
80. Luzieux, L.D. Origin and Late Cretaceous-Tertiary Evolution of the Ecuadorian Forearc. Ph.D. Thesis, ETH Zürich, Zürich, Switzerland, 2007.
81. Nisbet, E.; Pearce, J. Clinopyroxene Composition in Mafic Lavas from Different Tectonic Settings. *Contrib. Miner. Petr.* **1977**, *63*, 149–160. [[CrossRef](#)]
82. Leterrier, J.; Maury, R.; Thonon, P.; Girard, D.; Marchal, M. Clinopyroxene composition as a method of identification of the magmatic affinities of paleo-volcanic series. *Earth Planet. Sci. Lett.* **1982**, *59*, 139–154. [[CrossRef](#)]
83. Le Bas, M.J. The role of aluminium in igneous clinopyroxenes with relation to their parentage. *Am. J. Sci.* **1962**, *260*, 267–288. [[CrossRef](#)]
84. Beccaluva, L.; Macciotta, G.; Piccardo, G.B.; Zeda, O. Clinopyroxene composition of ophiolite basalts as petrogenetic indicator. *Chem. Geol.* **1989**, *77*, 165–182. [[CrossRef](#)]
85. Rollinson, H. *Using Geochemical Data: Evaluation, Presentation, Interpretation*, 1st ed.; Longman: Singapore, 1993; p. 352.
86. Hart, S.R.; Dunn, T. Experimental cpx/melt partitioning of 24 elements. *Contrib. Miner. Petrol.* **1993**, *113*, 1–18. [[CrossRef](#)]
87. Sun, S.S.; McDonough, W.F. Chemical and isotopic systematics of oceanic basalts: Implications for mantle composition and processes. In *Magmatism in the Ocean Basins*; Saunders, A.D., Norry, M.J., Eds.; Geological Society: London, UK, 1989; Volume 42, pp. 313–345.
88. Folk, R.L.; Andrews, P.B.; Lewis, D.W. Detrital sedimentary rock classification and nomenclature for use in New Zealand. *J. Geol. Geophys.* **1970**, *13*, 937–968. [[CrossRef](#)]
89. Litherland, M.; Klinck, B.A.; Oconnor, E.A.; Pitfield, P.E.J. Andean-trending mobile belts in the Brazilian shield. *Nature* **1985**, *314*, 345–348. [[CrossRef](#)]
90. Vallejo, C.; Soria, F.; Tornos, F.; Naranjo, G.; Rosero, B.; Salazar, F.; Cochrane, R. Geology of El Domo deposit in central Ecuador: A VMS formed on top of an accreted margin. *Miner. Depos.* **2016**, *51*, 389–409. [[CrossRef](#)]
91. Christophoul, F.; Baby, P.; Dávila, C. Stratigraphic responses to a major tectonic event in a foreland basin: The Ecuadorian Oriente Basin from Eocene to Oligocene times. *Tectonophysics* **2002**, *345*, 281–298. [[CrossRef](#)]
92. Spikings, R.A.; Crowhurst, P.V.; Winkler, W.; Villagomez, D. Syn- and post-accretionary cooling history of the Ecuadorian Andes constrained by their in-situ and detrital thermochronometric record. *J. S. Am. Earth Sci.* **2010**, *30*, 121–133. [[CrossRef](#)]
93. Pilger, R.H. Cenozoic plate kinematics, subduction and magmatism: South American Andes. *J. Geol. Soc.* **1984**, *141*, 793–802. [[CrossRef](#)]
94. Pardo-Casas, F.; Molnar, P. Relative motion of the Nazca (Farallon) and South America plate since Late Cretaceous time. *Tectonics* **1987**, *6*, 233–248. [[CrossRef](#)]

95. Sébrier, M.; Lavenu, M.; Fornari, M.; Soulas, P. Tectonics and uplift in the central Andes (Peru, Bolivia and northern Chile) from Eocene to present. *Geodynamique* **1988**, *3*, 85–106.
96. Sempéré, T.; Herail, G.; Oller, J.; Bonhomme, G. Late Oligocene-early Miocene major tectonic crisis and related basins in Bolivia. *Geology* **1990**, *18*, 946–949. [[CrossRef](#)]
97. Laubacher, G.; Naeser, C.W. Fission-track dating of granitic rocks from the Eastern Cordillera of Peru: Evidence for Late Jurassic and Cenozoic cooling. *J. Geol. Soc. Lond.* **1994**, *151*, 473–483. [[CrossRef](#)]
98. Hall, M.; Calle, J. Geochronological control for the main Tectono-Magmatic events of Ecuador. *Earth Sci. Rev.* **1982**, *10*, 215–239. [[CrossRef](#)]

**Publisher’s Note:** MDPI stays neutral with regard to jurisdictional claims in published maps and institutional affiliations.



© 2020 by the authors. Licensee MDPI, Basel, Switzerland. This article is an open access article distributed under the terms and conditions of the Creative Commons Attribution (CC BY) license (<http://creativecommons.org/licenses/by/4.0/>).